Available online at www.sciencedirect.com

ScienceDirect

Journal of the European Ceramic Society 31 (2011) 429–449

www.elsevier.com/locate/jeurceramsoc

Review

Study of the friction, adhesion and mechanical properties of single crystals, ceramics and ceramic coatings by AFM

J.J. Roa [a,*], G. Oncins [b,c], J. Díaz [b], X.G. Capdevila [a], F. Sanz [c,d], M. Segarra [a]

[a] University of Barcelona, Faculty of Chemistry, Department of Materials Science and Metallurgical Engineering,
C/ Martí i Franquès, 1, 08028 Barcelona, Spain
[b] Scientific-Technical Services of the University of Barcelona (SCT·UB), C/ Lluis Sole i Sabaris, 1, 08028 Barcelona, Spain
[c] Institut of Biongineering of Catalonia, C/ Josep Samitier 1-5, 08028 Barcelona, Spain
[d] University of Barcelona, Faculty of Chemistry, Department of Physical Chemistry, C/ Martí i Franquès, 1, 08028 Barcelona, Spain

Received 9 March 2010; received in revised form 13 September 2010; accepted 13 October 2010
Available online 19 November 2010

Abstract

This paper reviews commonly used methods of analyzing and interpreting friction, adhesion and nanoindentation with an AFM tip test data, with a particular emphasis of the testing of single crystals, metals, ceramics and ceramic coatings. Experimental results are reported on the friction, mechanical and adhesion properties of these materials.

The popularity of AFM testing is evidenced by the large quantity of papers that report such measurements in the last decade. Unfortunately, a lot of information about these topics is scare in the literature. The present paper is aimed to present the basic physical modelling employed and also some examples using each technique.

Keywords: Mechanical properties; Plasticity; Biomedical applications; Engine components

---

Contents

---

* Corresponding author.
E-mail addresses: jjrr_cons@hotmail.com, joanjosep_roa@ub.edu (J.J. Roa).

0955-2219/$ – see front matter © 2010 Elsevier Ltd. All rights reserved.
doi:10.1016/j.jeurceramsoc.2010.10.023

1. Introduction

1.1. Classical mechanism of friction

The study of friction and its implications in our world formally began with the experiments of Leonardo da Vinci (1452–1519) who was the first scientist that studied friction phenomena in a quantitative way.[1] He concluded that friction force (F_f) does not depend on the area of contact (A) and it is proportional to the mass of the slider (M_s). His observations lead to the first definition of friction coefficient (μ) as the direct relationship between F_f and M_s:

$$\mu = \frac{F_f}{M_s} \tag{1}$$

Leonardo found a μ value of 0.25 for all tested materials and this was considered as a universal constant for several centuries.

It was Guillaume Amontons (1663–1705) who rediscovered Leonardo's works about friction and took them a step further, proposing that F_f is proportional to the vertical force (F_v).[2] Finally, Charles Augustine de Coulomb (1736–1806) set the basis of the macroscopic friction theory as we know it today:

$$F_f = \mu F_v \tag{2}$$

He also established that F_f value is independent of velocity once motion starts, idea that was refined by Leonhard Euler (1707–1783),[3–5] who introduced the concept of *kinetic* and *static friction* for the first time; when the two sliding surfaces are in motion relative to each other, μ is called *kinetic friction coefficient* and the F_f value is the force that tries to counteract the pushing force that creates the sliding movement. In the case of two surfaces that do not move relative to each other, μ is called *static friction coefficient* and it is usually higher than the *kinetic* one. Now, according to these new concepts, F_f value must be considered as a threshold force. In other words, until F_f value is not surpassed by the pushing force, the sliding will not begin. As we can see, F_f defined by Coulomb does not depend on A. In this direction, John Theophilius Desanguliers (1683–1744) had previously proposed that adhesion force (F_a), which is the force needed to separate two bodies in contact, played a key role in the friction phenomena and that F_a was a function of A.

In 1954, as an attempt to discern the dependence between F_f and A, Bowden and Tabor proposed a solution for the area of contact dilemma[6]; not only did they establish that two bodies do not contact with their whole surface, but also that they do it by means of a finite number of small *asperities*. This new concept redefined the way of studying contacting surfaces and drove tribology towards the micrometric world. As a matter of fact, they theoretically demonstrated that

$$F_f = F_v^{2/3} \tag{3}$$

As a result, Amontons' laws were called into question again but not for long, as in 1957 Archard found the way to unify both the old and new theories[7]; in their works, Bowden and Tabor had considered that the number of asperities, which are proportional to the real A value, were independent on the applied F_v value. Archard considered that this assumption was not right and modelled the relationship between the number of asperities and F_v. Finally, he concluded that F_f and F_v values were proportional.

1.2. Mechanism of adhesion

The adhesion phenomenon is relevant to many scientific and technological areas and has become in recent years a very important field of study.[8] There are a number of theories on how adhesion work and there is little common agreement as to which theory is the most relevant for any particular bonding case. Based on the different approaches, many theoretical models of adhesion have been proposed, which together are both complementary and contradictory: Mechanical interlocking, electronic theory, diffusion theory, theory of boundary layers and interphases, adsorption (thermodynamic) theory and chemical bonding theories represent the best approaches to resume the different mechanism which explain the phenomena of adhesion.

It was not until 1922 that the Adhesives Research Committee of the DSIR made a similar challenging statement, which was quickly accepted by McBain[9] who, with his co-workers, made the first steps towards any theory of the fundamentals of adhesion and distinguished between "specific and mechanical adhesion. The theory considered that there were two kinds of adhesion, specific and mechanical. Specific adhesion involved interaction between the surface and the adhesive: this might be "chemical or adsorption or mere wetting," Specific adhesion has developed into the model we today describe in terms of the adsorption theory. On the other hand, the electronic theory of adhesion, proposed by Deryagin and Krotova[10] in 1948, proposed that an electron transfer mechanism between the substrate and the adhesive, having different electronic structures, can occur to equalize the Fermi levels. This phenomenon could introduce the formation of a double electrical layer at the interface permitting that electrostatic forces can contribute significantly to the adhesive strength. Complementary to this theory, in the theory of boundary layers and interphases the concept of interphase is introduced since Bikerman[11] demonstrate that alterations and modifications of the adhesive and/or adherent can be found in the vicinity of the interface leading to the formation of an interfacial zone exhibiting properties that differ from those of the bulk materials and however, the diffusion theory was originally associated with Voyutskii and other Russian workers.[12] Much of Voyutskii's original work was done on the self-adhesion (called autohesion) of unvulcanised rubber. It was extended to polymer adhesion, more generally, and to even the adhesion of polymers to metals. The theory postulates that the molecules of the two parts of the specimen interdiffuse, so that the interface becomes diffuse and eventually disappears. It was argued that the development of adhesion with time, the effects of molecular weight, of polarity, and of cross-linking all proved that the adhesion was associated with the interdiffusion of polymer chains. By contrast, the adsorption (thermodynamic) theory[13] states that adhesion results from intimate intermolecular contact between two materials, and involves surface forces that develop between the atoms in the two surfaces. According to this theory, in the event of intimate contact between the adhesive and the adherent, the adhesive strength arises as a result of secondary intermolecular forces at the interface since physical adsorption involves van der Waals forces across the interface. These involve attractions between permanent dipoles and induced dipoles. Finally, the chemical bonding theory[14] of adhesion invokes the formation of covalent, ionic or hydrogen bonds across the interface. It is easily understandable that chemical bonds formed across the adhesive–substrate interface can greatly participate to the level of adhesion between both materials. These bonds are generally considered as primary bonds in comparison with physical interactions, such as van der Waals, which are called secondary forces interactions.

Adhesion and interfacial phenomena are topics that are of great technological importance and scientific interest. These facts, together with the rapid development of analytical and computational tools, have led to many significant advances in these fields.

Areas in which interfacial and adhesion effects play an important, if not dominant, role include friction, wear, triboelectrification, surface contamination control in microelectronics, particle adhesion, and bioadhesion. Moreover, these fields pervade many technological disciplines, including pharmacology, agriculture, electrophotography, electronics packaging, semiconductor fabrication, and, of course, adhesives. Accordingly, the fields of adhesion and interfacial phenomena have become quite multidisciplinary in recent years.

Being one of the more prominent members of the family of scanning probe microscopies, atomic force microscopy (AFM) has provided[15] a number of highly interesting approaches during the last years, mostly dealing with the quantitative measurement of mechanical properties at the true nanoscale.[16–18] Measurements of surface–surface interactions at the nanoscale are important because many materials have unique properties at this range.[19] In general, AFM is attractive for studies at the fundamental level of single asperities, since the method is suitable for the detection of adhesion forces in nanometer scale contacts of real surfaces with high spatial resolution under pressures of up to several GPa.[20] With these new approaches at hand, one of the main challenges of modern tribology can be tackled, i.e., to develop a fundamental understanding of nanoscale contacts. In addition, ceramics cannot be easily deformed plastically, so they do not give rise to altered contact areas and pressures.

To summarize this brief section, three quite different reviews applicable to future developments in understanding adhesion physics involving plasticity are highly recommended. The first, by Pettifor[21], reviews materials modelling from the physics point of view and is hierarchical in concept. The second, by Li et al.,[22] reviews atomistic modelling of mechanical behaviour from a materials science perspective. Finally, and from a mechanics viewpoint, Curtin and Miller[23] emphasize the multi-scale modelling concept as complementary to hierarchical approaches.

1.3. Classical mechanism of nanoindentation

Mechanical testing has been extensively used for characterization and quality control of materials. Unfortunately, the results are not comparable between measurements performed at different scales and strongly depend on the experimental method.[24]

AFM has become a powerful tool to detect structural changes at the nanoscale and its popularity between materials science researchers keeps on rising.[25] Recently, AFM was used to study surface deformation during cyclic loading[26–31] and also to study the intrinsic properties of ceramic materials.[32] Furthermore, AFM can not only image with high resolution but also measure forces involved in deformation. As an example, Rodriíguez de la Fuente et al. demonstrated the usefulness of the tungsten tip of a scanning tunneling microscope (*STM*), a technique closely related to AFM, as an indenter and imaging tool on an Au (1 0 0) surface in ultrahigh vacuum (*UHV*).[33] In subsequent studies, indentations performed with an AFM were observed to induce dislocations in metals, which could be explained in terms of a screw dislocation loop mechanism.[34,35] In an early application of contact mode AFM, Harvey et al determined the surface shape after nanoindentation with an AFM tip and confirmed the validity of continuum models for the plasticity of indentations.[36] With the same method, Gaillard et al. were able to resolve the complex dislocation structure after indentation on MgO and LiF with a commercial spherical tip nanoindenter.[37,38] Teran Arce et al. performed nanoindentations on MgO (1 0 0) with an AFM tip and imaged the surface using tapping mode AFM.[39] In these experiments, they detected discrete discontinuity events in the experimental force–distance curves but no dislocation structure was identified in the surface topography.

Between the main drawbacks of AFM as a nanoindentation tool, we can consider the difficulty in measuring the real radius of the tip.[32] Nanoindentation is now widely used to investigate the mechanical properties of materials.[40,41] For crystalline materials, nanoindentation can be used to characterize the nucleation of dislocations during the initial stages of plastic deformation. Some dislocation events can be identified by characteristic discontinuities in the force–distance curves[42] called pop-in events. Atomistic simulations were performed in order to understand the mechanisms behind dislocation nucleation and indentation size effects.[43,44] However, there is a gap in length scale between the limited size of atomistic simulations, which usually address nanometer-scale indenters and only a few dislocations, and nanoindentation experiments, where micrometer-scale indenters are used and a remarkable number of dislocations are produced. Indentation processes based on AFM can contribute to bridge the gap between atomistic simulations and experiments by addressing the nanoscale, providing experimental data about the smallest features in plasticity. In these regions, plasticity must be accommodated by a homogeneous nucleation of dislocations rather than activated by Frank–Read sources.[45] Incipient plasticity has now been studied using AFM for indentation and imaging on a number of surfaces, including MgO (1 0 0),[39] Au (1 0 0),[46] Au (1 1 1),[46] KBr (1 0 0)[47] and Cu (1 0 0),[48] in both ambient and *UHV* conditions.

2. Contact physics

2.1. Physics of friction: a new era for tribology

The *asperity* concept led their creators to propose that the physical process of friction consisted on the creation and melting of microscopic contacts as the two surfaces slid, ultimately considering that mechanical wear was the origin of friction. Nevertheless, this explanation did not endure the confrontation with reality: there was friction even between surfaces that did not show any appreciable wear.

Israelachvili, a student in Tabor's lab, took his advisor's ideas a step further[47]: in order to experimentally measure the real *A* value between two surfaces, he developed the surface force apparatus (SFA).[48–50] The idea consisted in bringing into close contact two pieces of mica bent in perpendicular directions. This setup would ensure that the apparent *A* value would equal the real *A* one, as the two contacting surfaces did not show any asperity. Israelachvili confirmed that friction truly depends on the real *A* value and also confirmed the close relationship between F_f and F_a values.

In the 80s, Gary McClelland developed a model which successfully explained the wearless friction phenomena[51] that had been previously observed. He proposed that when two surfaces slide, the outer atoms vibrate due to the released energy. These vibrations, called *phonons*,[52] travel along the surface in the form of a mechanical wave and act as a physical obstacle for the sliding interfaces. Then, wearless F_f value is the necessary force to overcome the mechanical phononic wave, which eventually is dissipated as thermal energy. An interesting implication of this model is that the frequencies of the generated *phonons* play an important role; if the two surfaces resonate, F_f increases dramatically due to the consequent vibration amplitude enhancement. Furthermore, the phononic theory predicted a much more striking fact: if the phononic resonance between the two sliding bodies could be minimized in the absence of wear phenomena, F_f value would virtually drop to zero.[53]

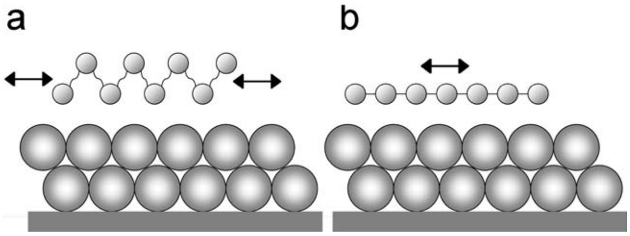

Fig. 1. *Phononic* friction. (a) liquid layer sliding on a solid surface. Due to the low interaction between liquid molecules, it is easy for them to commensurate with the solid substrate and increase F_f value. (b) Solid layer sliding on the substrate. The sliding layer cannot keep track with the substrate interatomic distance and slides with low F_f value.

The development of AFM by Binnig and Rohrer[15] let McClelland and his colleagues to test their theories. Briefly, AFM consists on a microfabricated probe ended with an extremely sharp tip that scans the sample, establishing an apparent *A* that can be in the nanometer range. McClelland tested his wearless friction theories just to find out that something was absolutely wrong; first of all, F_f was independent of F_v, which was in flagrant contradiction with all the previous theories. Besides, the shear stress (F_f/A) was incomprehensibly high. Quartz Crystal Microbalance measurements (QCM) performed by Jacqueline Krim observed another striking effect: F_f between noble gases and metals increases a lot in the presence of liquid.[54] Far from being an intuitive idea, as liquid are commonly believed to reduce friction, it fits acceptably well with the previous thesis about high F_f between commensurate surfaces; in fact, any liquid can be reasonably commensurate with a substrate due to the weak bonds between their molecules and its fluidity. Then, the liquid lets the two surfaces in contact to match more properly, as depicted in Fig. 1. A recent paper by Park et al.[55] shows how to control friction by tuning the potential landscape between the two sliding surfaces by applying an oscillatory F_v, in an attempt to provide a way to control adhesion and friction in sliding micro- and nanoelectromechanical systems (MEMS and NEMS, respectively).

This kind of experiments also explored the nature of electronic friction,[56] an interaction due to the electrical surface charges in the two sliding bodies. In this field of knowledge is remarkable the contribution by Park et al.[55] who showed that friction can be increased between doped silicon surfaces (standard base material for MEMS and NEMS) by applying an electric field, giving rise to extremely high and tuneable friction values that can be used to hold steady two surfaces in a controlled fashion with nanometric resolution.

2.2. Physics of adhesion

The role of adhesion was dramatically modified after the advent of three apparently disconnected events. Firstly, scanning probe microscopies and the capability to finely control exerted forces on samples, allowing atomic-scale measurement of adhesive point contacts. Secondly, computational materials science and the use of large scale atomistic simulations to examine the tribological properties of the surface of nanostructures, letting both the acquisition of data and the enhancement of theoretical understanding of adhesion and interfacial phenomena. Thirdly, the fact that microelectronics industry recently entered the nanoscale era has provided the driving force towards a better understanding of adhesion physics.[60] Gerberich et al. merged these separate challenges into an updating of how theoretical and experimental approaches are permitting new understanding of adhesion physics. He described some of the involved phenomena, the magnitudes and differences between the true work of adhesion, the work of separation and the practical work of adhesion. Similarly, on the experimental side, most studies have been hierarchical in nature and few considered examining the physics of adhesion across the length, time and temperature scales, now becoming available to AFM and nanoindentation instruments. Neither of these approaches, however, will be sufficient without appropriate multi-scale modelling that integrates the picture for complex engineering problems.

2.2.1. Macroscopic, atomistic and mesoscopic modelling

Consider the contact of two solids, α and β, in an environment equivalent to air. The work of adhesion per unit area as originally defined by Dupre and complemented by the IUPAC[57] corresponds to ${W_a}^{\alpha\beta\delta}$, which is the work done on the system when two condensed phases α and β forming an interface δ of unit area are reversibly separated to form unit areas of each of the $\alpha\delta$- and $\beta\delta$- interfaces.

$$W_a^{\alpha\beta\delta} = \gamma^{\alpha\delta} + \gamma^{\beta\delta} - \gamma^{\alpha\beta} \tag{4}$$

where $\gamma^{\alpha\beta}$, $\gamma^{\alpha\delta}$ and $\gamma^{\beta\delta}$ are the surface tensions between two bulk phases α and β; α and δ and β and δ, respectively.[58]

As a complement of the general approaches of W_a, the various levels of possible bonding, i.e., from electrostatic to full cohesion, are given and the approaches to modelling the physics of adhesion are manifold. Each of these is applied to the levels of adhesion in Fig. 2, with special emphasis on the higher adhesive stress regime.

2.2.1.1. Macroscopic modelling.

Macroscopic modelling is used for almost all elastic contacts and it is based on the contact mechanics established by Johnson.[59] Different theories have been used for explaining the different nature of the elastic contact,[60] i.e. JKR[61] and DMT[62] theories are applicable. A map due to Johnson[59] that sets the limits for the different contact mechanics models is reproduced in Fig. 3. Here, the normalized $\bar{F}$ value and a dimensionless scaling parameter, λ, are given by:

$$\bar{F} = \frac{F_a}{\pi W_{ad} R} \tag{5}$$

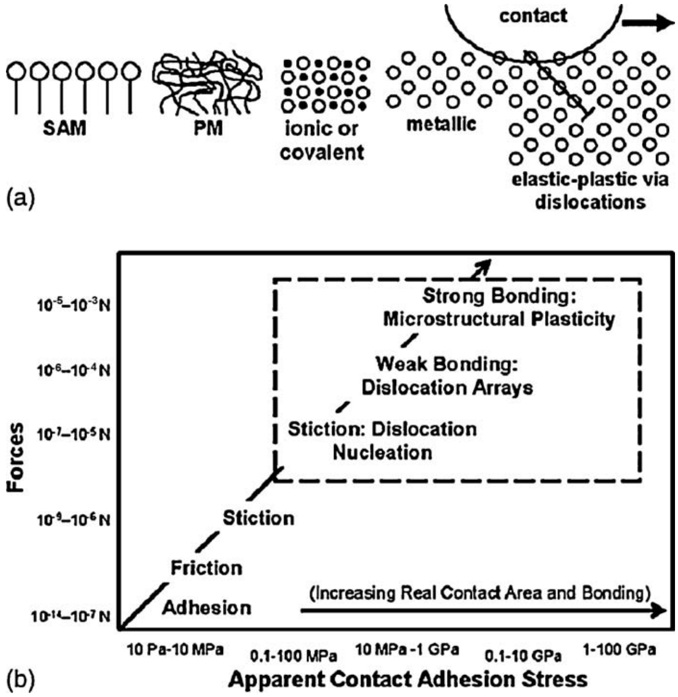

Fig. 2. (a) Friction or adhesive forces increases as contacts with self-assembled monolayers (SAMS), polymer microstructures (PM) such as pressure sensitive adhesives (weak) or block copolymers (strong) or ionic or metallic bonding without or with non-linear dissipation (dislocations) occur. Note that the schematic is not to scale for a 10^4 nm^2 contact. (b) A large range of contact forces can result when pulling the contact of (a) off any of the indicated surfaces. The contact adhesion stress increases due to increasing numbers of contacting asperities such that the real-to-apparent area ratio approaches unity or the bonding forces increase. In turn, the number of non-linear energy dissipation mechanisms increases with increased bond energy.

$$\lambda = 3.39\left(\frac{W_a^2 R}{K^2 z_0^3}\right)^{1/3} \tag{6}$$

$$K = \frac{4}{3}\left(\frac{1-\upsilon_1^2}{E_1} + \frac{1-\upsilon_2^2}{E_2}\right)^{-1} \tag{7}$$

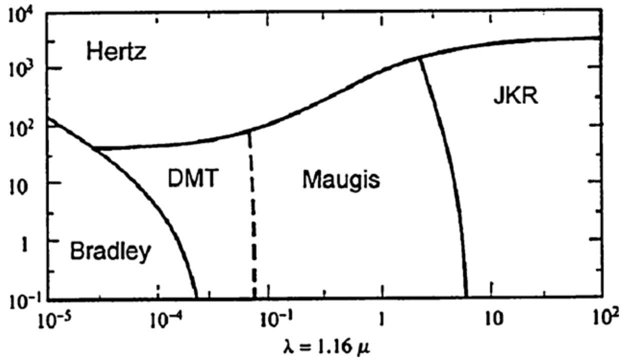

Fig. 3. JKR–DMT transition represented by Eqs. (5)–(7). The relationship between A value and F_v for an elastic sphere contacting a plane depends upon the range of attractive surface forces. A–load curves for the JKR limit (short-range adhesion), DMT limit (long-range adhesion) and an intermediate case are shown. All of these models approach the Hertz curve in limit $\gamma \to 0$ (no adhesion). Load and area are plotted in non-dimensional units as indicated.

where z_o is the equilibrium size of atoms in contact and K is an effective Young's modulus associated with two elastic bodies having Young's modulus E_1 and E_2 and Poisson ratios ν_1 and ν_2, respectively.[63]

When the pull-off takes place, the contact recession is like crack growth and the crack position advances with the remaining contact. This approach is applied for forces in the nanonewton regime for contacts smaller than 10 nm tip radius. For an elastic–plastic contact, Biggs and Spinks[64] proposed that

$$F_{ad} = \frac{3\pi W_a}{2(\pi H)^{3/2}} P^{1/2} \tag{8}$$

where H is the hardness or mean pressure and P is the pressure or applied force. For the same set of the above given parameters, again the F_a value is usually substantially less than 10 μN.

Other studies complement the macroscopic models; i.e. Suo et al.[65] conceptualized a continuum plasticity region contiguous to an elastic strip of height, 2D and dislocation-free, macroscopic modelling complemented by the elastic–plastic modelling at sharp interfaces. Furthermore, additional macroscopic modelling involved strain gradient plasticity models.[66–69] Nevertheless, as recognized by a large community, from the microscopic point of view, macroscopic modelling presents some lacks which can be complemented by atomic models.

2.2.1.2. Atomistic modelling. The main two types of atomistic modelling are those dealing with both structure and chemistry of interfaces and those dealing with dislocation structures at or near interfaces. These models need a previous consideration about phase boundaries;[70–72] there is some concern here since many, if not most, atomistic[73,74] and 'macroscopic atom' models[75] have shown to give energies greater than experimental values. Bennet et al.,[75] Siegel et al.[76,77] and Raynolds et al.[78] have studied the theoretical W_a, the former using a macroscopic atomistic model and the two latter using self-consistent density functional theory (DFT) calculations.

Several studies demonstrate that there seems to be a trend for interfacial energy to decrease with increasing misfit, where the misfit parameter is defined by ξ. This crude misfit parameter is given in terms of radii ($r\alpha$, $r\beta$) at the interface,

$$\xi = \frac{r_\alpha - r_\beta}{r_\beta} \tag{9}$$

with $r\alpha$ being the larger of the two species. On the other hand, other studies show a very weak dependence among the studied oxides and their corresponding metals.[74–79]

In an elegant and detailed study using first-principles calculations, Batyrev et al.[74] showed that the work of adhesion of Nb/sapphire interfaces could depend on the cleavage plane as well as on the terminating surface atoms prior to adhesion. Finally, other atomistic simulation approaches try to understand mesoscopic structures.[80,81]

2.2.1.3. Mesoscopic modelling. Mesoscopic refers to the middle-ground plasticity effect on de-adhesion. It is neither the microstructural effect on the work of separation at the atomistic end nor the continuum plasticity effect that might apply to far-field regions from the interface. There are two mesoscopic approaches which have dominated to date; one deals with simple, idealized arrays of a few dislocations that can be handled by interactive codes with either static[82] or dynamic conditions.[83] These have generally involved dislocation emission at the crack tip[82] or near from it.[83] The other type typically involves larger simulation codes with many external sources randomly placed by a Voronoi tessellation.[84] We talk about quasi-continuum models when a far field continuum region is modelled by finite elements.[85–87] They can include atomistic, microstructural and continuum plasticity in a single simulation. These and similar crack-tip source models[88–91] were generally directed towards cleavage phenomena in relatively brittle materials. For the adhesion subject at hand, only a few attempts at adapting this type of modelling have been made.[88,89]

With various theoretical components and computational approaches described, it is appropriate to next consider the experimental approaches for measuring the work of separation.

2.2.2. Normal force experimental techniques

Gerold et al.[92] discussed the magnitude of F_a the adhesion force experienced between two solid surfaces and concluded that is dependent on a number of factors, including temperature, relative humidity, and surface chemistry. One of the most important factors though is the real A value.[93] If the surfaces in contact are rough, then the real A value is composed of multiple asperity contacts. Also, adhesion-modifying agents, such as condensed liquids, fillers, and chemical additives, typically contribute directly to the asperity bond force, a key factor in order to gain greater insight into the mechanisms of adhesion. Unfortunately, the techniques that directly measure F_a between solid surfaces (scanning probe microscopies[94–96]) make the study of asperity adhesion difficult.

2.2.2.1. Force–distance curves. Fig. 4 exhibits the schematic of a typical force–distance curve obtained in AFM-force spectroscopy mode, i.e., a nanoindentation. When the AFM tip is far from the sample surface there is no cantilever deflection (Δ), as there is no interaction between the tip and the surface (Fig. 4(a)). Then, as the AFM probe moves towards the sample, a process known as jump-to-contact takes place; the AFM probe bends downwards due to van der Waals and water meniscus interactions which force the probe to contact the sample (Fig. 4(b)). As F_v value increases, the cantilever deflection also increases and the sample is compressed (Fig. 4(c)). During the unloading process, i.e., the AFM probe moving back to the initial position far from the sample, another process known as jump-off-contact appears (Fig. 4(d)), which is related with the F_a established between tip and sample during the contact.[101,102]

2.2.3. Mapping of multiphase systems

An obvious application area of AFM concerning adhesion measurements is the study of heterogeneous systems as ceramic films deposited onto substrates. Gerberich and Cordill[97] reported, W_a values for metal/ceramic and metal/semiconductor systems and complemented the work with a shorter review of adhesive organic contacts. Wang et al.[98] and Venkataraman

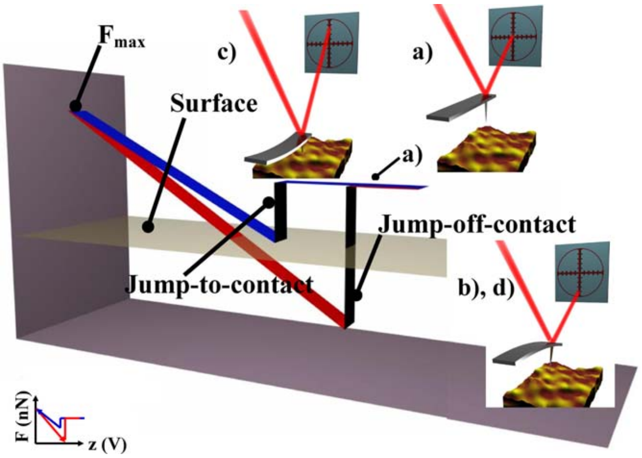

Fig. 4. Schematic of the AFM picoindentation procedure showing the different parts of a typical *F–z* curve, both in the loading and in the unloading process: (a) when the tip is far from the surface, there is no interaction between the AFM probe and the sample; (b) as the tip approaches the surface, it bends downwards due to attractive van der Waals forces, the water meniscus or electrostatic forces (jump-to-contact); (c) due to the hard contact between the sample and the surface, the tip bends upwards and the sample is elastically compressed; and (d) during the unloading process, adhesion forces arise between the tip and the sample (jump-off-contact).

et al.[99] reported on successful adhesion studies of metal/ceramic interfaces with increasing metal-film thickness. For example, in Ti/Al_2O_3 interfaces, W_a value as measured by both microscratch and four-point bending increased from 0.3 to 90 J m^{-2} as thicknesses increased from 100 nm to 100 μm, a factor of 300-fold increase in toughness.

F_a of micro and nanoscale particles to surfaces is of tremendous interest in a wide range of industrial and civilian applications. Nevertheless, the lack of experimental studies is obvious, although some exceptions are found; Cooper et al.[100] and Larson et al.[101] studied the F_a value in modelled rough alumina particle and SiO_2, respectively, and Muir et al.[102] presented an interaction force study of alumina fibers in water with coadsorbed polyelectrolyte.

The F_a of particles with different radii can be reasonably well described by an adsorbed layer model,[103,104] i.e., neglecting deformation and roughness. Nevertheless, the surface of real, crystalline spheres, even those made as ideal as possible, always show some defects[105] and to describe the particle interaction of a real, usually rough particle, an appropriate model is necessary since geometry fluctuations in the nanometric range affect F_a value strongly. Because molecular van der Waals forces rapidly decrease with separation distance, the geometry and the density of matter in the interaction volume dominate the particle interaction. This phenomenon is properly expressed by the density theorem.[106] The contact volume inside a 200–300 nm spacing between the interacting partners is the most relevant for particle interaction and F_a value can be calculated by a rod model where the total particle F_a is divided into surface forces and bulk forces (see Fig. 5)[107].

However, the quantity of matter inside the interaction volume of the contact can be increased due to deformations and can affect the F_a value. Unfortunately, *A* value of hard oxide particles is difficult to determine experimentally and has been theoretically calculated using the JKR approach[61] or the Hertz theory by means of the adhesive van der Waals pressure.[108] Therefore, the rod model is able to predict reasonably an accurate F_a between particles but it cannot describe the force as a function of separation at small distances (<10 nm). One possible reason is that the applied static view of the adhesion process might not be relevant. For this reason, a revision developing molecular dynamic (MD) calculations is required to understand adhesion

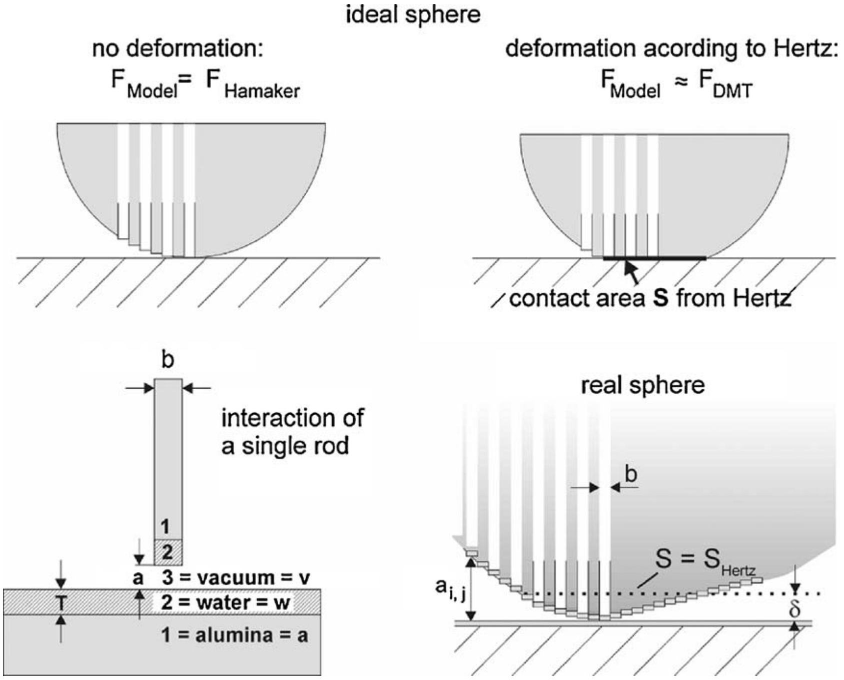

Fig. 5. Rod model used to calculate F_a between particles. Validation by an ideal sphere (top) and application to real particles (bottom).

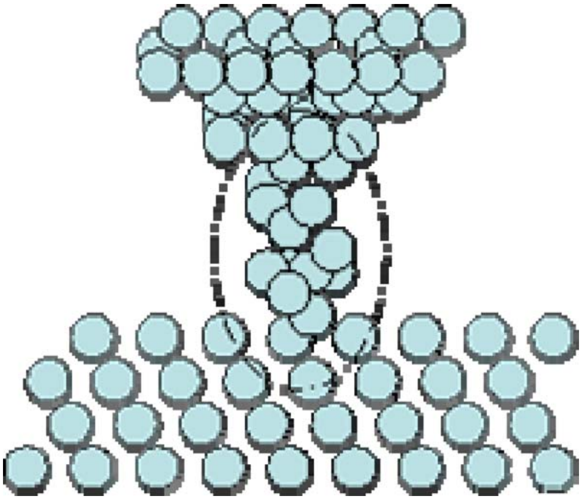

Fig. 6. Nanoparticle in contact with a surface in the pull-off stage. The formation of a nanowire in the contact zone just begins.

on a molecular level. In MD simulations performed after contact, the interaction force is attractive due to rearrangement of the ions. As shown in Fig. 6, large deformations occur and a long nanowire is formed in the pull-off stage. The formation of nanowires was also observed in MD studies of gold by Landman et al..[109] However, as Götzinger and Peukert[107] confirm, no appropriate model is available yet that allows a description of this phenomenon (step-wise rip off). The understanding of the material rearrangement together with the development of an appropriate water model seems to be a key to understanding particle adhesion in the future.

2.3. *Physics of nanoindentation*

2.3.1. *Improving force calibration*

A desire for accurate, traceable, small forces measurement is emerging within the International Organization for Standardization (ISO) task groups and ASTM International technical committees that work on instrumented indentation standards.[110] The most common approach to force measurement consists on a calibrated mass in a known gravitational field or deadweight force, which is universally accepted as the primary standard of force. The smallest calibrated mass available from NIST is 1 mg having a relative uncertainty of about 10^{-4}. In principle, smaller masses could be calibrated, but they would be difficult to handle.[111] Moreover, the relative uncertainty tends to increase inversely with mass,[111] potentially resulting in uncertainties that are of similar magnitude to deadweight forces in the range of nanonewtons. Besides, forces in this range can be measured using the electrical units defined in the International System of Units (SI) and linked to the Josephson and quantized Hall effects in combination with the SI unit of length.[112,113]

The mechanical work required to change either the overlap or the separation of two electrodes in a one-dimensional capacitor while maintaining constant voltage is

$$dW = F \cdot dz = \frac{1}{2} \cdot V^2 \cdot dC \tag{10}$$

where dW is the change in energy (also, known as mechanical work), F is the force, dz is the change in the overlap or separation of the electrodes, V is the electric potential across the capacitor, and dC is the change in capacitance. Thus, F can be obtained by measuring V and the capacitance gradient, dC/dz:

$$F = \frac{1}{2} \cdot V^2 \cdot \frac{dC}{dz} \tag{11}$$

This result indicates that the electrostatic force can be constrained and measured in a fashion that is traceable to the SI and with accuracy high enough to warrant consideration as a primary standard of force in this regime.

2.3.2. *Improving tip shape calibration*

A number of recent efforts have been made to improve tip shape calibration for nanoindentation technique.[114–120] These efforts have included material-independent methods of tip shape calibration using AFM[114–118] and alternative procedures using indentation of reference materials.[114,119,120] Roa et al.[32] developed a method to obtain the correct AFM probe radii. The AFM probe radii were reconstructed using specific software (SPIP, *Image Metrology*, *Horsholm*, *Denmark*) and a SiO_2 test grating with nanometrically sharp spikes (NiOProbe, Aurora Nanodevices, Nanaimo, Canada). The probe radius (R) was measured before and after each mechanical test in order to ensure that the tip shape did not change due to plastic deformation under the applied F_v value, which would invalidate the calculated Young's modulus. Fig. 7 exhibits the last 20 nm of the AFM tip apex before and after indentation experiments performed at a F_v value of 200 nN. Fig. 7(a) and (b) shows that the AFM tip did not undergo plastic deformation during the indentation experiment, where a F value of 200 nN was applied around 50 and 60 times.[32]

The AFM tip shows the same radius (approximately 9 nm) and general shape before and after the indentation process. For this reason, it can be inferred that under the exertion of the cited F_v value, the AFM tip only deforms elastically. This result led us to firmly believe that the force–distance curves obtained for the different materials studied render E values that are not biased by any tip contribution.

2.3.3. *Mechanical characterization at picometric scale*

Nanoindentation with an AFM tip is a powerful tool which let us obtain quantitative, reliable and reproducible E values. However, very little information about this theme is available in the literature.[32] Nowadays, it is widely accepted that a correct understanding and characterization of the E values during the working lifetime of advance ceramic samples is critical to any desired structural application. Nanoindentation by means of AFM and force spectroscopy has several advantages over standard methods (such as nanoindentation using a Berkovich tip indenter, micro- or macroindentation technique, Bending, and other) when it comes to the quantification of E values for ceramic samples. Firstly, the measurements are extremely local and can be performed on different areas so as to average the mechanical properties of the sample. Secondly, measured E value is depth-sensing so it allows characterization of a material at different penetration depth values (δ). Finally, it is not necessary to

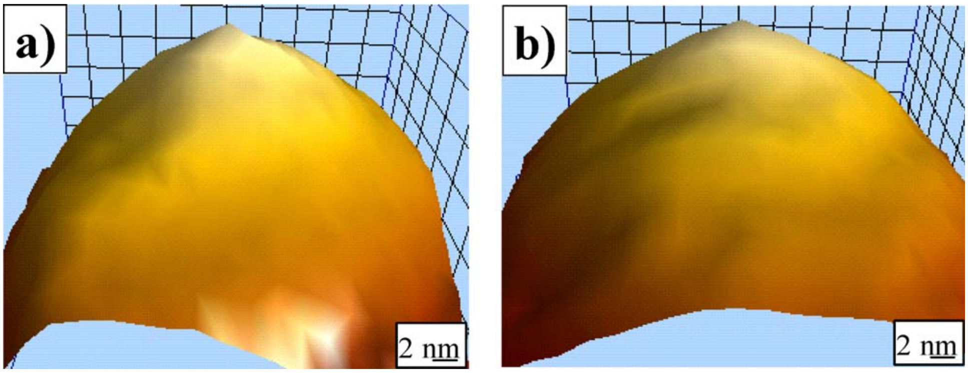

Fig. 7. Software reconstruction images of the AFM tip, (a) before the picoindentation test at 200 nN and (b) after the picoindentation test at 200 nN.

observe the residual imprint with an AFM or scanning electron microscope (SEM). All of these advantages mean that nanoindentation performed by Nanoindenter (Agilent Technologies), CSM$^+$ or Hysitron Triboscope allow us to extract hardness and Young's modulus for bulk and coatings materials with a limited thickness of 50 nm. However, nanoindentation with an AFM tip is a suitable and reliable technique for measuring E values while applying F_v values ranging from a few nN down to the pN level.

The main principle of nanoindentation technique is widely explained in Section 1.3. Nanoindentation by means of AFM-FS has several advantages compared to standard methods regarding the quantification of E value for YBaCuO samples.

F is calculated as (see Fig. 8(b))

$$F = k_v \cdot \Delta \tag{12}$$

where Δ is the cantilever deflection, defined as

$$\Delta = \frac{\Delta V}{S} \tag{13}$$

where ΔV is the increment in photodetector vertical signal as the tip contacts the sample and S is the sensitivity, which is the slope of the contact region of a force–distance curve performed on a rigid sample.

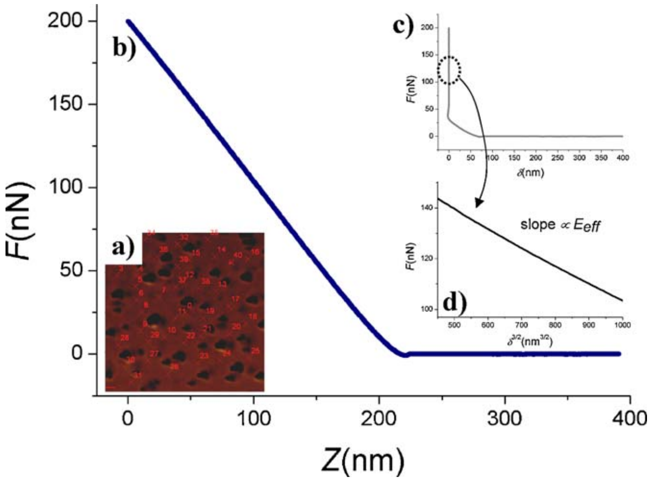

Fig. 8. Images of the different steps taking place during the picoindentation process. (a) AFM image with 40 different spots, (b) force–distance curve, (c) force–penetration curve, and (d) force–penetration$^{3/2}$, where E value can be calculated using Hertzian equations.

δ value due to the exerted F value is evaluated as (see Fig. 8(c))

$$\delta = z - \Delta \tag{14}$$

where z represents the piezo-scanner displacement in the axis perpendicular to the sample plane. After puncturing the sample, a topographic image was captured in order to ensure that sample had not undergone any plastic deformation.

Force–distance curves obtained at a certain F_v value were analyzed using the Hertz model in the elastic region[121–123] by means of Eq. (15) (see Fig. 8(d)[32]):

$$F_v = \left(\frac{3}{4} E_{eff} \sqrt{R}\right) \delta^{3/2} \tag{15}$$

where E_{eff} is the effective E value and can be obtained using the following relation:

$$\frac{1}{E_{eff}} = \frac{1-\nu^2}{E} + \frac{1-\nu_i^2}{E_i} \tag{16}$$

where ν is the Poisson ratio. Subindex i corresponds to the mechanical properties of the SiO$_2$ AFM probe ($E_i = 76$ GPa[124] and $\nu_i = 0.17$[125]).

3. Quantification of mechanical properties of single crystals, ceramics and ceramic coatings using AFM

3.1. Examples of friction

3.1.1. Diamond single crystals, diamond coatings and diamond-like carbon coatings for MEMS and NEMS

In the last years, the awakening of MEMS and NEMS, has led to the development of new nanotribological tools in order to test the performance of these systems. Besides, the surface processes as friction and adhesion are extremely important design factors. MEMS and NEMS are usually made out of silicon due to the extensively studied microfabrication processes developed for this material but it turns out to be a bad candidate in terms of wear and adhesion, as mobile parts tend to get stuck and degrade very fast, partly due to the high hydrophilicity of silicon oxide. In these scenario, diamond has become one of the best candidates in order to coat silicon surfaces, as C–C bond is 1.8 times stronger than Si–Si bond, has a much higher thermal conductivity (dissipation of energy during sliding is faster), its wear rate is 10^4 times lower, it is biocompatible and has a tailorable and stable surface chemistry.[126] It is remarkable the extremely low μ value of near-frictionless carbon coatings, as low as 0.001, and their outstanding wear rates better than diamond.[127] Diamond thin film technology has been greatly improved in the last years[128,129] and it is a candidate to reduce wear processes in silicon MEMS, which are controlled by high friction induced cracks, while friction itself is mainly controlled by the presence of dangling or adsorbate-passivated bonds. The first attempts to measure friction at the nanoscale where performed with the development of the Scanning Electron Microscope (SEM) tribometer,[130] which is basically a slider inside a vacuum chamber where the wear tracks can be SEM-visualized and the pressure of gasses controlled. In this context, the formation of dangling bonds after the desorption of adsorbates increases the μ value, while the presence of H_2 and the consequent saturation of surface bonds reduce μ value. This effect was also seen for diamond single crystal (1 1 1) surfaces in UHV, where μ value was found to be two orders of magnitude smaller in the presence of H_2.[131] In the field of molecular dynamics (MD) simulations, experiments for diamond surfaces at 80%, 90% and 100% H_2 saturation, showed that, the lower the saturation degree the more tribochemical reaction between the AFM tip and the sample at lower vertical forces.[132] This experiment introduced applied force on the sample as an important sample functionalization parameter, the higher the functionalization degree with ambient molecules, the higher the μ value and the lower the wear resistance. In the same line, density functional theory (DFT) calculations by Qi et al.[133] showed how water dissociates into –OH and –H on a diamond-like carbon film (DLC) surface, where –OH groups form covalent bonds with carbon atoms and Gardos also proposed water as a perfect lubricant for diamond and silicon surfaces.[134]

Surface orientation has proved to be an important factor when it comes to tribology. By means of simulations, Çagin et al. proposed that crystal surfaces sliding in different directions give rise to different μ values, extremely sensitive to the area of contact and the presence of asperities. In the case of diamond single crystals, macrotribological measurements showed that crystal orientation and sliding direction have a strong effect,[126] while in the case of nanotribology by AFM no effect was found, supposedly by the avoidance of wear at the atomic scale. A pioneer experiment performed in 1992[135] between an H-terminated diamond sample with two different crystallographic surfaces and a diamond AFM tip showed qualitative differences due to changes in crystal lattice and orientation and also showed the presence of stick-slip phenomenon; This mechanical instability at the atomic scale has been shown in a wide variety of samples and thought to arise from the surface potential periodic landscape of the sample, which is tracked by the AFM tip. This process dissipates a high quantity of energy in the form of heat and friction and different approaches have been devised to reduce it. Basically, obtaining an incommensurate interface reduces the energy loss and this can be achieved by means of the presence of certain gases between the sliding surfaces. This is the case of methane, which seems to dampen the vibrational excitation of a diamond slider and reduces the transference of energy to the other side of the interface.[136] A remarkable friction anisotropy effect due to sample orientation was shown in an experimental (AFM) and simulation (MD) work for diamond (0 0 1) and ($2 x 1$) surfaces.[137]

The first quantitative nanotribological study of ultrananocrystalline diamond (UNCD) was performed by Sumant et al.[138] UNCD thin layers are formed by pitless 5 nm diameter diamond grains (*mainly sp^3 bonds*) separated by narrow boundaries where there is a certain quantity of sp^2 C–C bonds. Friction measurements were performed using an AFM on the flat underside of UNCD layers after etching away the silicon substrate, rendering surfaces with a RMS roughness of 0.9 nm. UNCD Young's modulus is similar to the value for single crystal diamond, as well as its μ value (0.03 in air[139]). Friction experiments were performed scanning a WC-coated AFM tip in contact mode in a direction perpendicular to that of the main cantilever axis in order to observe the twisting of the cantilever, which is proportional to friction force (see Fig. 9). The work of adhesion between the tip and the silicon substrate was 115 mJ/m^2 and 59 mJ/m^2 for the UNCD-coated sample. Both friction and adhesion work were greatly reduced after treating the UNCD surface with hydrogen plasma, which resulted in a diminution of dangling bonds and in a reduction of the sp^2 hybridization in favour of the sp^3, as well as a reduction in C–O bonds.[131] The presence of sp^2 bonds had been previously proved to promote bonding between sliding surfaces by means of MD simulations.[140] After hydrogen plasma treatment, an adhesion work of 32–36 mJ/m^2 was measured, similar to the 10 mJ/m^2 observed for the same kind of AFM tips on H-terminated single crystal diamond (1 1 1) in UHV, where it was proposed that this energy was due to pure van der Waals interactions.[141]

Diamond-like carbon films[142] (DLC) are also widely studied as surface coatings for their outstanding mechanical properties. Nevertheless, as they have different ratios of sp^2 and sp^3 bonding, tribological properties can be varied and they are highly dependent on the degree of –H termination.[143] Experimental AFM results with diamond coated tips show that μ value increases with the presence of hydrogen and hardness and wear performance of the coating worsen. Nevertheless, macroscopic experiments suggest that there can be an optimal –H content. Different methods have been devised to control the ratio of sp^3 bonding in DLC layers, such as the microwave plasma chemical vapour deposition (MPCVD)[144] and the pulsed laser deposition (PLD).[143] With this last technique, DLC coatings with 34 and 53% of sp^3 bonding were achieved and AFM experiments with Si_3N_4 tips showed that, as Young's modulus increases with sp^3 content, μ value remains unchanged. Complementarily, MD simulations by Gao et al.[145] showed that not only the sp^3 bonding ratio is important, but also the 3D structure of the surface and the bulk chemistry of the sliding interfaces.

There is an interplay between humidity and DLC nanotribological properties, when sliding a Si_3N_4 tip on a DLC surface, friction increases with humidity but adhesion remains more or less constant.[146] It is proposed that water increases the shear

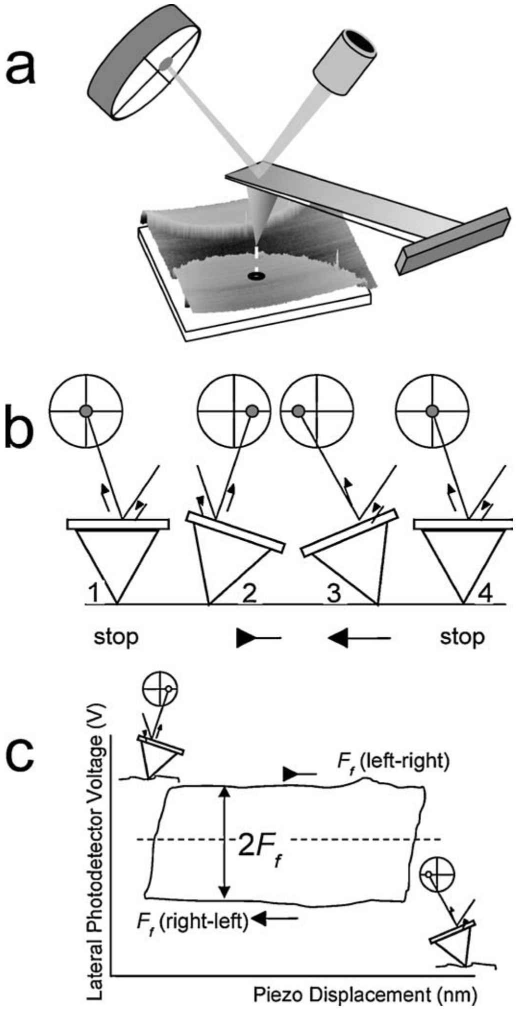

Fig. 9. (a) Schematics of an AFM. The cantilever deflection is detected by a laser that is reflected on a photodetector, which translates the laser spot movement into surface topography. (b) Scheme of the operating bases of the friction force microscope. The scanning direction is perpendicular to the main cantilever axis to enable the cantilever torsion during sliding. The figure shows a front tip view while performing a friction loop. (1) The tip lays still on the surface. (2) The probe scans to the right and the cantilever lateral deflection is recorded in the photodetector. (3) The probe scans to the right and the signal in the photodetector changes. (4) Scanning stops. (c) Shape of a typical friction loop. The *Y* axis represents the lateral photodetector signal as the tip slides on the sample surface, which is proportional to friction force.

strength of the contact but it is also suggested that the idea of a water meniscus being formed between the tip and the sample during sliding can be inaccurate. Besides, hydrogenated DLC films have proved to degrade in the presence of water[147] while single crystal diamond tribological performance is really poor in dry conditions.[131] A recent study by Konicek et al. deals with the effect of humidity in the friction response of UNCD samples vs. a UNCD slider;[148] it is well known that diamond shows a remarkably low friction in humid environments,[147] while showing a reverse behaviour in dry conditions. The low friction response is attributed to two different processes: first of all, a graphitization of the sliding surfaces,[149] i.e., rehybridization of sp^3 bonds to sp^2 as graphite is the stable form of carbon at room conditions. This process can be promoted during friction because the energy barrier of the rehybridization is lowered by shear and heat released during sliding;[149] Secondly, a passivation of the dangling surface bonds due to the effect of water and H_2. By means of X-ray absorption fine structure (NEXAFS) and X-ray photoelectron emission microscopy (X-PEEM), Konicek et al. concluded that passivation is the main responsible of nanotribological behaviour of a UNCD–UNCD interface, as the chemical analysis of the sliding interface do not show signs of sp^2 bonding. These results are supported by simulation works showing that the dissociation of H_2 and H_2O molecules on a diamond surface are energetically favourable,[150] fact that is experimentally confirmed by the increase of C–O and C=O bonds in the sliding surfaces after conducting the friction experiment.

3.1.2. SiC single crystals, ceramics and coatings

SiC has become one of the most interesting advanced ceramics and it is used in electronics due to its capability to be doped and its wide band gap, as a structural material and specially as high abrasion resistance coating for MEMS, NEMS and cutting tools.[151] Nevertheless, recent studies showed that oxidation of SiC leads to the formation of a SiO_2 surface layer with much lower wear resistance and tribological performance than the underlying material.[152–154] In order to study this phenomenon down to the nanoscale, Pöhlmann et al. used an AFM diamond tip to scratch the surface of a SiC single crystal and test its wear resistance.[155] After applying a vertical force of 60 μN on single scanning lines of 5 μm at a sliding velocity of 10 μm/s, they concluded that the wear track is slightly deeper in SiC C-face than in the SiC Si-face. This trend also repeats on thermally treated samples, where wear tracks are deeper due to the thicker SiO_2 layer grown on top of the sample. They concluded that the oxidation rate of the SiC Si-face is slower than that of the SiC C-face and that the oxide layer thermally grown degrades the tribological performance of the SiC single crystal. More recent MD works dealt with the mechanism of elastic–plastic deformation of SiC in great detail.[156] Noreyan and Amar[157] simulated the sliding of a rectangular indenter on a Si-terminated SiC single crystal, revealing a sample wear mechanism mainly due to ploughing and a remarkable single crystal orientation anisotropy in scratch hardness, μ value and dependence of μ value with indentation depth. The scratching process promotes the amorphization of the material under the slider and the extent of this process depends on the sliding speed. The authors propose that at higher sliding speeds, the sliding steady-state temperature increases and the material becomes softer, fact that explains the observed diminution of μ value and scratch hardness.[158]

3.1.3. Titanium dioxide coatings

Titanium dioxide has become an important material in a variety of fields that range from pigments to solar cells[159] but it is the field of biocompatibility[160] that gives to the nanotribological properties of this material a key performance role. Previous mechanical studies were performed in the past in the micro[161] and in the nanoscale,[162] as is the case of the work by Piwonski[163] They measure the wear response and COF of TiO_2 layers deposited on silicon wafers as a function of the level of porosity by means of AFM. Basically, the scratch tests show that wear is maximum at a medium level of porosity and minimum when the porosity is low. In fact, no wear is detected for non-porous samples, which is in accordance with previous studies.[162] The authors propose that the observed wear resistance vs. porosity behaviour is due to the thicker pore walls of low porosity samples, which increase the mechanical resistance of the sample. Besides, as the material becomes more plastic when it exhibits high porosity, COF increases, mainly due to the higher area of contact between the AFM tip and the sample.

3.1.4. SiO_2 and Al_2O_3 surfaces

SiO_2 has become a candidate to be one of the main structural materials for MEMS and NEMS and has been widely used in the microelectronics industry for years. The development of miniaturized sliding parts demands accurate friction measurements in order to improve the performance and durability of SiO_2 parts. A pioneer work from Scandella et al.[164] studied the frictional response of SiO_2 surfaces, both thermally and natively grown, and compared it with the response of H-terminated Si, a passivating strategy widely used in Si cleaning and preparation which remains stable for several hours in room conditions.[165] Measurements performed in dry N_2 atmosphere with a Si_3N_4 tip, passivated with a SiO_x thin layer at room conditions,[166,167] showed no difference in the μ value for thermally and natively grown SiO_2 surfaces but reported a noticeable increase in μ value for H-terminated Si surfaces (0.6 ± 0.1 and 0.3 ± 0.1, respectively; reported μ values correspond to F_v values in the range 0–30 nN). μ values for SiO_2 are consistent with previously reported data (0.25–0.35 for polisilicon on Si[168] and 0.21–0.38 for polisilicon on Si_3N_4[169]). Scandella et al. concluded that the observed differences in frictional response do not respond to adhesion effects but to the formation and destruction of Si–O–Si bonds during the sliding of the AFM tip and also remarked that traces of water present in the chamber could play an important role in the chemistry of the contact. This specific effect was thoroughly studied by Binggeli and Mate[170] by performing tribological tests on Si surfaces coated with a native SiO_2 layer as a function of humidity in a bidirectional force microscopy. They reported a μ value of 0.5 for measurements performed at 0–75%RH and a progressive tip wear due to sliding. Nevertheless, higher humidity values led to μ values of 0.25 and negligible tip wear after a number of cycles, concluding that water molecules reduce the shear strength of the SiO_2-probe junctions and promote a smoother sliding. To further explore the influence of surface chemistry, they coated the SiO_2 surface with a 1.5 nm thick hydrophobic perfluoropolyether layer, obtaining a μ value of 0.35 at low humidity and 0.25 at high humidity. Further contact experiments demonstrated that the polymer-coated surface greatly reduce the size of the water meniscus in the tip-sample contact and that high humidity values reduce friction response for both hydrophilic and hydrophobic surfaces. It is worth to mention the work by Opitz et al.,[171] who was able to control the thickness of water deposited on SiO_2 surfaces down to the nm level by means of STM measurements. A precise control of the amount of water present on the sample surface revealed that the lowest frictional response between a Si AFM tip and a SiO_2 sample is obtained in the absence of water. In this regime, only cohesive (bonding) forces are present between the surfaces. As humidity increases, double layers of water molecules form on the hydrophobic surfaces, especially around the contact region; this phenomenon increases the shear strength and viscosity of the contact leading to a higher friction regime. The properties of these specific water structures had been reported before and demonstrated to be remarkably different from those of bulk water.[172,173] As humidity increases and coats the sample surface forming 1–3 nm thick layers, friction response is highly dominated by capillary effects. Interestingly, Opitz et al. report that water does not gather in the sliding interface but around it when a nanocontact is established, stressing that cohesive forces between the AFM tip and the sample surface are always present but masked by strong capillary forces. This fact complements previous microscopic tests where water was demonstrated to be confined in the sliding interface, loosing degrees of freedom and behaving as a two-dimensional liquid.[174] In a later paper, Opitz et al.[175] studied the frictional response and chemical modifications that SiO_2 undergo under the presence of small amounts of water in UHV in more detail. They concluded that silanol terminated surfaces show a high surface energy when no water is present on the surface (formation of Si–O–Si bonds between tip and sample), that this surface energy noticeably decreases at higher water pressures of 8×10^{-9} mbar due to a nanolubricant effect and that finally the surface energy increases again at higher water contents due to capillary forces. In fact, they proposed that the sample surface undergoes important chemical changes, as –OH groups initially present in the surface desorb in the absence of water forming siloxane groups, appearing again as water content increases. Nanotribological tests performed on siloxane-terminated SiO_2 surfaces (hydrophobic) show that water promotes the formation of silanol groups only in the sliding interface, indicating that SiO_2 surface chemical modifications may be temperature and pressure mediated.

Al_2O_3 tribology is of capital importance as it is applied in microelectronics recording devices that imply sliding interfaces during long periods of time. Bhushan et al.[176] performed wear tests on Al_2O_3 coatings deposited on single crystal Si (1 0 0) wafers by means of a ball-on-flat reciprocating tribometer. The obtained μ values range from ca. 0.2 for F_v values between 2 and 25 mN, increases up to 0.6 between 15 and 18 mN of applied F_v values and then decrease to a steady value of 0.45 for F_v values up to 25 mN. SEM investigation of the tested regions showed the presence of an unexpected ductile deformation and surface chipping. Friction experiments by AFM performed on Al_2O_3 surfaces performed on wear tracks after pin-on-disc tests in humid environment showed that wear is highly reduced in the presence of water due to the formation of aluminium hydroxide by combination of the fine Al_2O_3 debris accumulated along the track with water.[177] Molecular dynamics simulations performed at the atomic level[178] demonstrated that the friction arisen between two hydroxylated α-Al_2O_3 surfaces greatly depends on the sliding velocity; as proposed, atomic friction is due to atomic vibration of the interface atoms and also due to interdigitation of these atoms as both surfaces slide, giving rise to a certain temperature increase. This temperature, lower in the layers below the surfaces due to poor heat conductivity, is accompanied by a disturbance of the potential energy minimum of atoms, i.e., their equilibrium state. As sliding velocity increases, F_f value decreases as there is less time to dissipate heat and let the atoms to return to the cited minimum energy state. Experimental tests performed at variable humidity conditions by means of AFM reported μ values of 0.2 for Al_2O_3 at 20%RH and values as high as 0.6 at 70%RH.[179] Interestingly, the authors also report that μ values remain constant when F_v values ranging from 250 to 900 nN are applied at humidity levels below 50% but that they decrease in a hyperbolic fashion for high F_v values at high humidity tests.

3.1.5. *Ceramic in aqueous environment: a matter of charge*

When immersed in aqueous environment, oxides have a certain surface charge. Its value depends on the different pK_a values of the involved surfaces and the pH of the medium.[180] The amount of charge and the quantity of ions present in the solution determine the nature of the electrostatic double layer (EDL) that forms on top of the sample and that counterbalances its charge up to a certain extent. Apart from the EDL, the presence of structured water has also to be considered, as water molecules are structured on the surfaces and around the ions and originate strong short range repulsive forces which can mask the attractive van der Waals interactions.[181] Considering the case of α-alumina colloidal dispersions, which was studied by Yilmaz et al.,[182] their surface can protonate and deprotonate depending on the pH (AlO^- at basic pH and $AlOH_2{}^+$ at acidic pH). The measurement of friction forces between colloidal particles is of great interest as it defines how particles flow over one another, process which proved to be highly dependent on the electrostatic structure around the involved sliding surfaces. To do that, Yilmaz et al attached a micrometric sapphire (0 0 0 1) sphere at the end of an AFM cantilever and studied the frictional response of a α-alumina surface in basic medium as a function of electrolyte concentration. They concluded that μ value decreases from 0.54 to 0.27 as ionic KCl concentration ranges from 10^{-3} to 1 M. They attribute this fact to the higher electrostatic interactions that arise between surfaces as salt concentration increases and the thickness of the EDL decreases in accordance. This data is supported by similar works.[183,184] The rheological properties of water trapped between two ceramic surfaces (in this case, mica) was studied by Raviv and Klein[181] By means of surface force balance studies, they proved that the fluidity of water between two sliding pieces of mica held at 1 nm distance at high salt concentration (>0.1 M) keeps on being the same as bulk water and that this compressed fluid is the origin of a strong electrostatic repulsion between the mica surfaces.

3.2. *Examples of adhesion*

The AFM tip is used as a pull-off adhesion tester, measuring the force required to pull a specified surface contact point between tip and sample. Unequal pulling force during testing caused by uneven adhesive bond lines and surfaces can result in random, unexplainable readings. Nevertheless, adhesion measurements by means of force spectroscopy can be uniformly distributed over the tested surface, obtaining an average response that minimizes the effect of spurious results. One of the main applications of this technique is the study of the general effect of surface hydrophobicity/hydrophilicity on the adhesion behaviour; if both substrate and AFM tip are hydrophilic, water meniscus around the tip promotes large F_a values.[185] In contrast, if the sample surface is hydrophobic, F_a value is reduced due to the high interfacial tension in the sample-tip system, which is indicative of low compatibility. Moreover, during the adhesion measurements another effects we should to take into account as electrostatic forces, van der Waals, or hydration forces as can be widely described in Ref. 186.

3.2.1. *AFM substrates: mica and silicon oxide*

Leite et al.[187] measured F_a value (mean pull-off force in force spectroscopy experiments) between an AFM tip and two types of substrate (muscovite mica and silicon wafers) and concluded that F_a strongly depends on both the surface roughness and type of material since the dispersion is higher for the rougher substrate. Indeed, it is well-known that mechanical surface properties in the nanoscale, such as friction and adhesion, are affected by the surface topography,[188] where smooth samples show lower F_a values.[189]

Pöhlmann et al.[190] and Zum Garh et al.[191] tried to better understanding the tribological mechanisms of self-mated SiC sliding pairs under far different operating conditions with contact areas ranging from the nanoscale to the millimeter scale, different roughness and oxidation state of SiC surfaces and variable humidity conditions, both in vacuum and in air. The experimentally obtained μ values suggest a strong dependence on the chemical composition (carbon content of the oxide layer, etc.), the type of surface (hydrophilic or hydrophobic surfaces), and the amount of water surrounding the AFM-probe. Binggeli and Mate[192] carried out a study in order to quantify the F_a value of SiC as a function of the humidity for hydrophilic and hydrophobic. This paper reveals that strong capillary interaction take place around the tip for hydrophilic surfaces. However, an abnormal behaviour takes place for hydrophobic surfaces of silicon oxide covered with a perfluoropolyether lubricant. In this case, the water capillarity formation around the tip is suppressed.

3.2.2. *Spherical ceramic particles: SiO_2 and Al_2O_3 nanoparticles*

One of the first works where scanning probe microscopies were applied to measure the nanoscale adhesion properties of nanoparticles was reported by Zou et al.,[193] who studied the silica nanoparticle-textured (SNPT) and silicon oxide films (SOF) surfaces. The SNPT and the SOF samples were characterized by AFM using a diamond tip of nominal R value = 40 nm. In the case of the SNPT surface, the nanoparticles were barely distributed on the surface and only the tallest ones were selected for the adhesion measurements. The effective radius of curvature of the contact was determined by the radius of curvature of the silica nanoparticle (<100 nm) and the results show the presence of single asperity contacts between the diamond tip and the surface. In the case of the SOF surface, the radius of curvature of the contact was determined by the diamond tip, as SOF samples are extremely flat. In these last conditions, it was shown that the F_a value increases almost linearly with the R value.[194]

In order to study the effect of adsorbed layers on F_a value, Götzinger and Peukert[107] coated alumina particles that were previously glued on SiO_2 cantilevers with water, CO_2, N_2, Kr, Ar and different length hydrocarbons. The advantage of using particles instead of a sharp AFM tip is that the interaction volume and A can be more precisely defined during the experiments. The measured interaction forces were compared with calculated forces using the Hamaker concept[195,196] and a rod model that includes an adsorbed surface layer and the experimentally determined interaction volume. It turned out that calculated F_a values, neglecting deformation, are smaller than measured ones.

As alumina and SiO_2 particles are high surface energy materials, in ambient conditions the surface energy tends to be reduced by one up to two orders of magnitude because of water and hydrocarbon adsorption. This fact highly affects the particle adhesion properties and has to be taken into account when establishing the experimental conditions.[109] Ducker et al.[197] in 1992, developed an AFM-related technique employing AFM which can be used to measure forces on small particles or fibers. This technique is suitable to study materials of a high variety of compositions and geometries; in that specific work, the authors studied the surface forces acting between colloidal particles in aqueous solution.

3.2.3. *Biocompatible ceramics: calcium hydroxyapatite*

Calcium hydroxyapatite is the primary mineral component of all mammalian skeletal and dental tissues, i.e. bone, dentine, cementum and enamel. The crystal properties were investigated by means of AFM by Kirkham et al.[198,199] showing that, during early development, crystal surfaces display morphological features resembling regular bead-like swellings. By contrast, at later stages regular patterning was seen. In addition to this study, Robinson et al.[200] investigated adhesion properties of calcium hydroxyapatite by means of AFM and chemical force microscopy (CFM), using both hydroxyl and carboxyl modified AFM tips. Experimental adhesion maps indicate that F_a value per unit area increases when pH decreases, presumably due to increased protonation of the crystal surface. Below pH 6.6 F_a values become erratic due to destabilisation of the crystal surfaces and adherence of material to the AFM tip.

3.3. *Example of plastic deformation using nanoindentation*

3.3.1. *(0 0 1)-KBr crystal*

Fig. 10, taken from the work of T. Filleter and coworkers,[47] shows nanoindentation experiments performed in a KBr-(0 0 1) surface with AFM tips with different radii of 7 nm and 30 nm. The force–distance curves for each experiment exhibit characteristic discontinuities when a critical F_v value is reached. For the smaller tip, several discontinuities take place during the loading process up to 150 nN. As expected, the jump heights in this

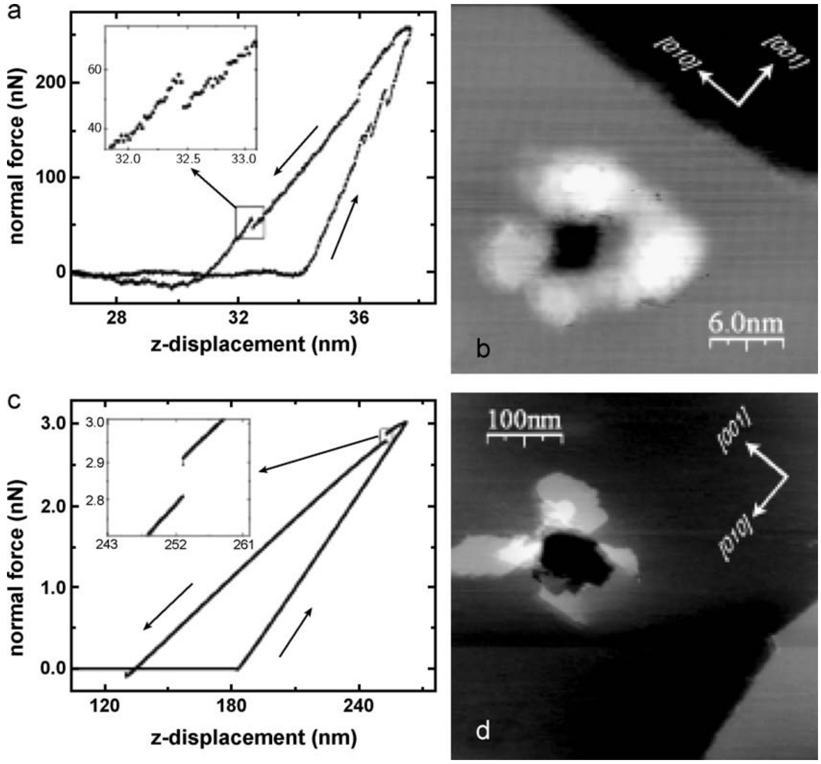

Fig. 10. Surface topography and force–distance curves for indentations performed with two different tip radii. (a) Force–distance curve recorded during indentation with a 7 nm tip radius. Not the single occurrence of a jump-out event detailed in the insert. (b) Topography image recorded after this indentation. (c) Force–distance curve recorded during indentation with a 30 nm tip radius. The inset shows the only discontinuity in this curve, with a height of about 3 nm. (d) Topography image recorded after this indentation, the lateral size of the dislocation structure is significantly large than in (b). A large hysteresis effect is observed in both force curves which is caused by a large retraction of the sample before indentation as a safeguard to conserve the tip shape.

low-force regime correspond with the indentation of monatomic steps. In the unloading portion of the force–distance curve a single discontinuity of reversed direction can be recognized,[47] probably indicating the relaxation of a formerly slipped plane. For the higher tip, discernible discontinuities appear in load ranging from 2.5 to 3 μN, both in the loading and in the unloading portion of the force–distance curve. The discontinuities in Fig. 10(c) show steps that are 3.1 nm high that correspond to about nine atomic layers of KBr. Moreover, the topographic images identify where the dislocation loops created in the indentation process intersect the surface. In Fig. 10(b) and (d), the authors[47] propose that during the first stages of dislocation nucleation the lateral extension of the dislocation structure depends on the tip *R* value; the smaller its value, the more extended the initial dislocation structure.

3.3.2. (1 0 0)-MgO crystal

Fig. 11(a) exhibits a force–distance curve recorded while performing an indentation corresponding to a monoatomic layer. The discontinuity, identified by the large peak in the derivative of the loading curve (*see the arrow*), takes place about 21 nm after the tip has come into contact with the surface. Furthermore, the sign of the peak in the derivative curve indicates an abrupt increase in the rate of penetration of the tip as it presses the surface. Therefore, the mentioned discontinuity is interpreted to correspond with the rupture of one MgO atomic layer while the tip penetrates the surface.[201] The cavity shown in Fig. 11(b) has a mean diameter of about 16 nm and its depth coincides with the measured height of the MgO (1 0 0) monatomic step to the right of the cavity. The debris resulting from the indentation adopts a planar disk shape with a height that corresponds to one monatomic layer and a volume which is similar to that of the cavity after tip convolution is taken into account.[201]

Fig. 12(a) exhibits the force–distance curve and corresponding derivative of a 5.5 nm deep indentation (Fig. 12(b)). The different discontinuities, identified by peaks in the force–distance derivative, are also observed in the force–distance curves discontinuity and are interpreted as atomic planes being expelled by the AFM tip during the nanoindentation process. Creation of dislocations was not observed on the surface of the MgO crystal during the experiments.[201]

The loading curve in Fig. 13 exhibits two regions separated by an abrupt jump. The first region (I) extends from 0 to a depth ca. 2 nm and it is interpreted to correspond to the elastic behaviour of MgO crystal. This region can be modelled using Hertzian theory for a parabolic shaped tip indenting a plane.[201] The second region (II), which begins with the onset of the first discontinuity, corresponds to plastic deformation of the crystal. The first region of the unloading curve [region (III)] corresponds to elastic recovery of the crystal during the unloading process.

Plastic deformation is characterized by the sequence of discrete events in region (II). The width of region (II) lies between 5 and 5.5 nm and each discrete event detected in this region correlates with the number of atomic layers expelled by the tip during the indentation process (the number of ejected atomic layers is shown above each discontinuity of the loading curve in Fig. 13). In this case, the total number of expelled layers (18), inferred from the force–distance curve, agrees with the depth of the cavity (Fig. 12(b)).

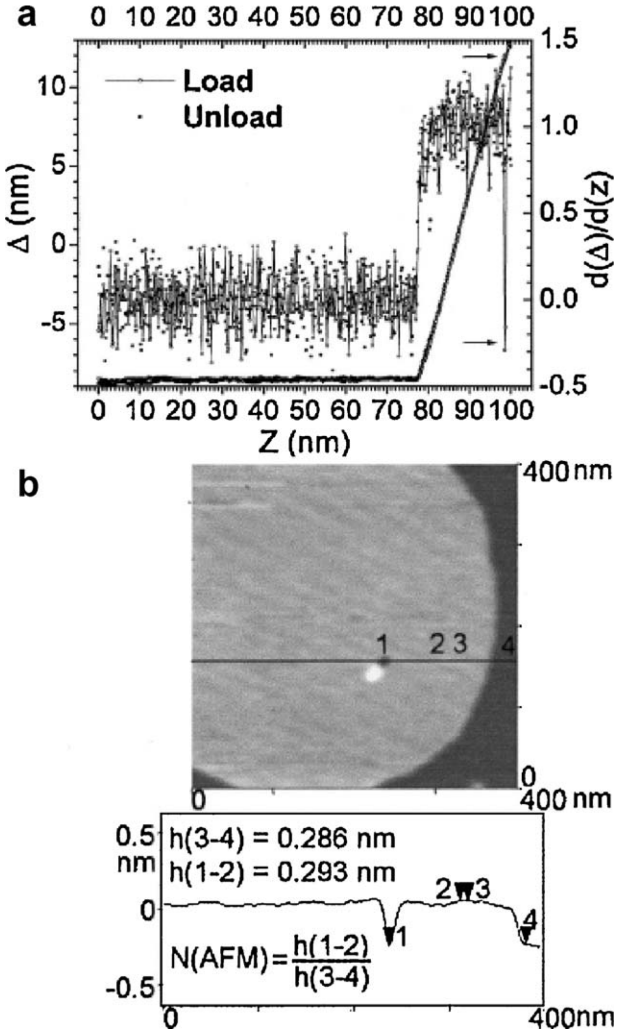

Fig. 11. (a) Force–distance curve and its derivative for a monatomic deep indentation. Loading is indicated by straight lines and unloading by full squares. Arrows indicate the discontinuity in the force–distance curve and the corresponding peak in its derivative. (b) AFM image and cross section corresponding to the created cavity. Note that the depth of the cavity is approximately the same as the monatomic step height to the right.

3.4. Examples of elastic deformation using nanoindentation

YBCO materials show high critical current density and high trapped magnetic field at cryogenic temperatures (*liquid nitrogen, 77 K*). However, practical applications of these types of materials are often limited by their poor mechanical performance, especially at cryogenic temperatures. Hence, mechanical properties such as hardness, microhardness, elastic modulus, etc., are crucial for industrial applications of these kinds of materials. These parameters are really important to employ this type of materials for in the current transport, motors, flywheels, etc. $YBa_2Cu_3O_{7-\delta}$ (YBCO or Y-123) presents a heterogeneous structure of Y-123 (which is the superconducting phase) and Y_2BaCuO_5 (which is the non-superconducting phase). YBCO samples prepared by the Bridgman and TSMG technique render

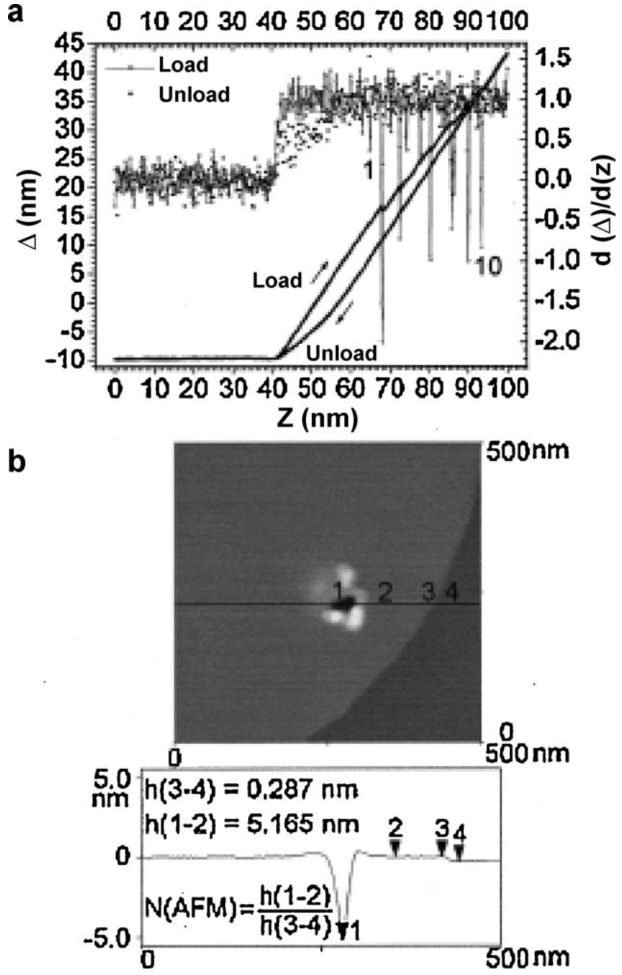

Fig. 12. (a) Cantilever deflection–distance curve and its derivative for a picoindentation. Loading is indicated by straight lines and unloading by full squares. (b) AFM image and cross section of the picoindentation performed in (a), where the cavity depth corresponds to 18 monatomic layers.

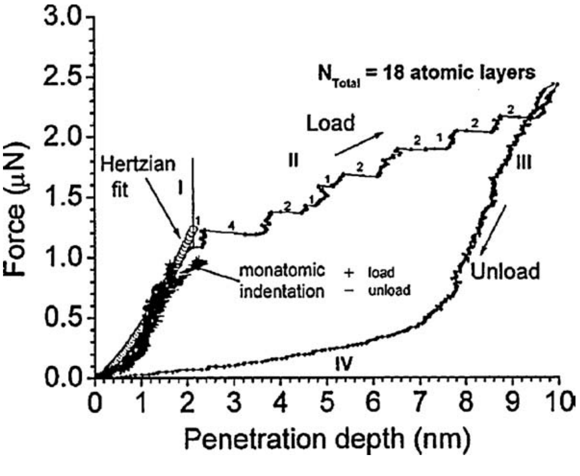

Fig. 13. The discontinuities in the force–distance curve correspond to the peaks in the force–distance curve derivative present in 12(a). The inferred number of atomic layers expelled by the tip is indicated above each discontinuity. The depth measured from the nanoindentation curve corresponds to 18 atomic layers and agrees with the cavity depth shown in 12(b).

higher *E* values for Y-211 than for Y-123 phases. This fact could be due to different reasons: (i) Y-211 phase ionic bond is stronger than Y-123 (related to the different melting point of the two different phases: $T_{\text{Y-123}} \sim 1010\,^{\circ}\text{C}$ and $T_{\text{Y-211}} \sim 1200\,^{\circ}\text{C}$[202]), and/or (ii) the high anisotropy confined onto the (0 0 1) plane of the Y-211 phase creates dislocations and residual stresses inside the particle due to its compressive state during the solidification process, which generates microcracks in the surrounding matrix.[203] These microcracks drastically affect the microstructure acting as nucleation sites.[203]

When the YBaCuO samples textured by self-flux technique are doped with Ca and Sr, *E* value drastically decreases due to the ionic and crystallographic radius of the different doping elements. Then, as the Y^{3+} is substituted by a Ca^{2+} cation in the YBaCuO unit cell, an increment of the unit cell volume is produced. In this case, *E* value reduction can be attributed to different effects; (i) the ionic and crystallographic radii are different, $r_{Ca^{2+}} > r_{Y^{3+}}$, and (ii) the different elements present a different coordination number.[204] Both phenomena promote the creation of vacancies, which in turn originate dislocations that are the origin of a high density of surface defects.[203] A similar phenomenon takes place when the Ba^{2+} is substituted by Sr^{2+}; nevertheless, as Ba^{2+} and Sr^{2+} present the same coordination number, *E* value for Sr^{2+} doped samples is a bit higher (~6%) than in the case of Ca^{2+} doping agent. In conclusion, dopants modify YBaCuO crystallographic parameters and produce an *E* value reduction. The different values presented in this section are in correct agreement with several previous works performed by Roa et al.[205] by nanoindentation technique.

4. Conclusions

The present paper seeks to present and discuss the most relevant results concerning the analysis of friction, adhesion and nanoindentation with an AFM tip of single crystals, metals, ceramics and ceramic coatings at the nanoscale in order to provide a clear overview of ceramic nanomechanics to researchers entering the field and a useful guide to those seeking for experimental advice. Besides, the theoretical framework necessary to interpret the results concerning the different nanomechanics disciplines is also reviewed.

Nanomechanics is a field of knowledge that moves forward at fast pace due to new technical developments, especially related to scanning probe microscopies; these developments provide faster and more accurate results that eventually will lead to a full understanding of mechanics at molecular and atomic scale. The works reviewed in this paper show that there is a reasonable correspondence between macro- and nanometric friction results, although the latter are much more influenced by surface phenomena as water meniscus, electrical charges and intermolecular interactions. Such is also the case of adhesion measurements, where the constant development of new models to calculate the true area of contact between surfaces is leading researchers to conclude that the true area of contact is much smaller than expected due to the presence of nanoasperities. These considerations are also important in the field of nanoindentation, where forces in the range of piconewtons can be applied in order to study individual movement of atoms in crystal structures and the propagation of surface defects as dislocations and point defects.

Acknowledgment

The authors acknowledge the Nanometric Techniques Unit of the Scientific-Technical Services of the University of Barcelona for technical support.

References

1. Dowson D. *History of tribology*. London: Longmans; 1979.
2. Amontons G. *De la Resistance causée dans les machines. Memoires de l'Academie Royale*. Amsterdam: Chez Gerard Kuiper; 1706.
3. Dowson D, Coulomb CA. *J Lubr Technol* 1785;**100**:148–52.
4. Euler L. Sur le frottement des corps solides. *Mem Acad Sci Berl* 1748;**4**:122–30.
5. Euler L. Sur la diminution de la résistance de frottement. *Mem Acad Sci Berl* 1762;**18**:256–60.
6. Bowden FP, Tabor D. *The friction and lubrication of solids. Part I.* Oxford: Clarendon Press; 1954.
7. Archard JF. Elastic deformation and the laws of friction. *Proc R Soc Lond A* 1957;**243**:190–205.
8. Shultz J, Nardin M. In: Pizzi A, Mittal KL, editors. *Theories and mechanism adhesion. Handbook of adhesive technology*. 1994.
9. McBain BV, Hopkins DG. *J Phys Chem* 1925;**29**:188.
10. Deryagin BV, Krotova NA. *Dokl Akad Nauk SSSR* 1948;**61**:849.
11. Bikerman JJ. *The science of adhesive joints*. New York: Academic Press; 1961.
12. Voyutskii SS. *Autohesion and adhesion of high polymers*. Interscience; 1963.
13. Copeland LE, Young TF. *Solid surfaces chapter 37*; 1961. p. 348–56.
14. Plueddemann EP. In: Ishida H, Kumar G, editors. *Molecular Characterization of Composites Interfaces*. New York: Plenum Press; 1985. p. 17.
15. Binnig G, Quate CF, Gerber C. Atomic force microscope. *Phys Rev Lett* 1986;**56**:930–3.
16. Bhushan B, editor. *Handbook of Micro/Nano Tribology*. New York: CRC Press; 1999. p. 371.
17. Meyer E, Overney RM, Dransfeld K, Gyalog T. *Nanoscience: friction and rheology on the nanometer scale*. Singapore: World Scientific; 1998.
18. Colton RJ, Engel A, Frommer JE, Gaub HE, Gewirth AA, Guckenberger R, et al. *Procedures in scanning probe microscopies*. New York: Wiley; 1998.
19. García R, Pérez R. Dynamic atomic force microscopy methods. *Surf Sci Rep* 2002;**47**(6–8):197–301.
20. Carpick RW, Salmeron M. Scratching the surface: fundamental investigations of tribology with atomic force microscopy. *Chem Rev* 1997;**97**(4):1163–94.
21. Pettifor DG. Electron theory in materials modelling. *Acta Mater* 2003;**51**:5643–73.
22. Li J, Ngan AHW, Gumbsch P. Atomistic modelling of mechanical behaviour. *Acta Mater* 2003;**51**:5711–42.
23. Curtin WA, Miller RE. Atomistic/continuum coupling in computational materials science. *Model Simul Mater Sci Eng* 2003;**11**:R33–68.
24. VanLandingham MR. Review of instrumented indentation. *J Res Natl Inst Stand Technol* 2003;**108**:249–65.
25. Ma J. AFM study of the morphology and micro-strain of slip bands in twin under cyclic deformation. *Mater Sci Eng A* 2007;**457**:63–8.
26. Cretegny L, Saxena A. AFM characterization of the evolution of surface deformation during fatigue in polycrystalline copper. *Acta Mater* 2001;**49**:3755–65.
27. Man J, Obrtlik K, Blochwitz C, Polak J. Atomic force microscopy of surface relief in individual grains of fatigued 316L austenitic stainless steel. *Acta Mater* 2002;**50**:3767–80.
28. Man J, Petrenec M, Obrtlík K, Polák J. AFM and TEM study of cyclic slip localization in fatigued ferritic X10CrAl24 stainless steel. *Acta Mater* 2004;**52**(19):5551–61.
29. Schwab A, Meibneri O, Holste C. Atomic force microscopy of slip lines on the surface of a fatigued nickel single crystal. *Philos Mag Lett* 1998;**77**:23–31.
30. Risbet M, Feaugas X, Guillemer-Neel C, Clavel M. Use of atomic force microscopy to quantify slip irreversibility in a nickel-base superalloy. *Scr Mater* 2003;**49**:533–8.
31. Cretegny L, Saxena A. Evolution of surface deformation during fatigue of PH 13-8 Mo stainless steel using atomic force microscopy. *Fatigue Fract Eng Mater Struct* 2002;**25**:305–14.
32. Roa JJ, Oncins G, Dias FT, Capdevila XG, Vieira VN, Schaf J, et al. AFM as an alternative for Young's modulus determination in ceramic materials in elastic deformation regime. *Ultramicroscopy*. Submitted, 2010.
33. Rodriguez de la Fuente O, Zimmerman JA, Gonzalez MA, Figuera J, Hamilton JC, Pai WW, et al. Dislocation emission around nanoindentations on a (0 0 1) fcc metal surface studied by scanning tunneling microscopy and atomistic simulations. *Phys Rev Lett* 2002;**88**:036101/1–4.
34. Carrasco E, Gonzalez MA, Rodríguez de la Fuente O, Rojo JM. Analysis at atomic level of dislocation emission and motion around nanoindentations in gold. *Surf Sci* 2004;**572**:467–75.
35. Carrasco E, Rodríguez de la Fuente O, Gonzalez MA, Rojo JM. Dislocation cross slip and formation of terraces around nanoindentations in Au (0 0 1). *Phys Rev B: Condens Matter Mater Phys* 2003;**68**:180102/1–4.
36. Harvey S, Huang H, Venkataraman S, Gerberich WW. Microscopy and microindentation mechanics of single crystal iron-3 wt.% silicon. Part I. Atomic force microscopy of a small indentation. *J Mater Res* 1993;**8**:1291–9.
37. Gaillard Y, Tromas C, Woirgard J. Study of the dislocation structure involved in a nanoindentation test by atomic force microscopy and controlled chemical etching. *Acta Mater* 2003;**51**:1059–65.
38. Gaillard Y, Tromas C, Woigard J. Pop-in phenomenon in MgO and LiF: observation of dislocation structures. *Philos Mag Lett* 2003;**83**:553–61.
39. Teran Arce PFM, Riera G, Gorostiza P, Sanz F. Atomic-layer expulsion in nanoindentations on an ionic single crystal. *Appl Phys Lett* 2000;**77**:839–41.
40. Johnson K. *Contact mechanics*. Cambridge, UK: Cambridge University Press; 1987.
41. Fischer-Cripps AC. *Nanoindentation*. New York: Springer; 2004.
42. Kiely JD, Houston JE. Nanomechanical properties of Au (1 1 1), (0 0 1), and (1 1 0) surfaces. *Phys Rev B: Condens Matter Mater Phys* 1998;**57**:12588–94.
43. Li J, Vliet KV, Zhu T, Yip S, Suresh S. Atomistic mechanisms governing elastic limit and incipient plasticity in crystals. *Nature* 2002;**418**(6895):307–10.
44. Knap J, Ortiz M. Effect of indenter-radius size on Au (0 0 1) nanoindentation. *Phys Rev Lett* 2003;**90**:226102/1–4.
45. Lorenz D, Zeckzer A, Hilpert U, Grau P, Johansen H, Leipner HS. Pop-in effect as homogeneous nucleation of dislocations during nanoindentation. *Phys Rev B: Condens Matter Mater Phys* 2003;**67**:172101/1–4.
46. Asenjo A, Jaafar M, Carrasco E, Rojo JM. Dislocation mechanisms in the first stage of plasticity of nanoindented Au (1 1 1) surfaces. *Phys Rev B: Condens Matter Mater Phys* 2006;**73**:75431/1–7.
47. Filleter T, Maier S, Bennewitz R. Atomic-scale and dislocation nucleation in KBr. *Phys Rev B* 2006;**73**:155433/1–10.
48. Israelachvili JN. Adhesion forces between surfaces in liquids and condensable vapors. *Surf Sci Rep* 1992;**14**:109–59.
49. Israelachvili JN, McGuiggan PM. Adhesion and short-range forces between surfaces. 1. New apparatus for surface force measurements. *J Mater Res* 1990;**5**:2223–31.
50. Israelachvili JN. Liquid dynamics in molecularly thin-films. *J Phys Condens Matter* 1990;**2**:SA89–98.
51. Mate CM, McClelland GM, Erlandsson R, Chiang S. Atomic-scale friction of a tungsten tip on a graphite surface. *Phys Rev Lett* 1987;**59**:1942–5.

52. Popov VL. Electronic and phononic friction of solids at low temperatures. *Tribol Int* 2001;**34**:277–86.
53. Socoliuc A, Gnecco E, Maier S, Pfeiffer O, Baratoff A, Bennewitz R, et al. Atomic-scale control of nanometer-sized contacts. *Science* 2006;**313**(5784):207–10.
54. Krim J, Solina DH, Chiarello R. Nanotribology of a Kr monolayer—a quartz-crystal microbalance study of atomic-scale friction. *Phys Rev Lett* 1991;**66**:181–4.
55. Park JY, Ogletree DF, Thiel PA, Salmeron M. Electronic control of friction in silicon pn junctions. *Science* 2006;**313**(5784):186–186.
56. Budakian R, Putterman SJ. Correlation between charge transfer and stick-slip friction at a metal–insulator interface. *Phys Rev Lett* 2000;**85**:1000–3.
57. PAC, 1972, 31, 577. *Manual of symbols and terminology for physico-chemical quantities and units, appendix II: definitions, terminology and symbols in colloid and surface chemistry*, p. 598.
58. *IUPAC compendium of chemical terminology*. 2nd ed; 1997.
59. Johnson KL. Mechanics of adhesion. *Tribol Int* 1999;**31**:413–8.
60. Fraxedas J, Garcia-Manyes S, Gorostiza P, Sanz F. Nanoindentation: toward the sensing of atomic interactions. *Proc Natl Acad Sci* 2002;**99**(8):5228–32.
61. Johnson KL, Kendall K, Roberts AD. Surface energy and the contact of elastic solid. *Proc R Soc Lond A* 1971;**324**:301–13.
62. Derjaguin BV, Muller VN, Toporov YP. Effect of contact deformations of the adhesion of particles. *J Colloid Interface Sci* 1975;**53**:314–23.
63. Salmeron M, Folch A, Neubaurer G, Tomitori M, Ogletree DF. Nanometer scale mechanical properties of Au (1 1 1) thin films. *Langmuir* 1992;**8**:2832–42.
64. Biggs S, Spinks G. Atomic force microscopy investigation of the adhesion between a single polymer sphere and a flat surface. *J Adhes Sci Technol* 1998;**12**:461–78.
65. Suo Z, Shih CF, Varias AG. A theory for cleavage cracking in the presence of plastic flow. *Acta Metall Mater* 1993;**41**:1551–7.
66. Huang Y, Zhang L, Guo TF, Hwang KC. Near-tip fields for cracks in materials with strain-gradient effects. In: Willis JR, editor. *Proc. IUTAM symp. nonlinear analysis*. Cambridge: Kluwer; 1995. p. 231–42 [physics of adhesion 2199].
67. Lipkin DM, Clarke DR, Beltz GE. A strain-gradient plasticity model of cleavage fracture in plastically deforming materials. *Acta Mater* 1996;**44**:4051–8.
68. Jiang H, Huang Y, Zhuang Z, Hwang KC. Fracture in mechanism-based strain gradient plasticity. *J Mech Phys Solids* 2001;**49**:979–93.
69. Huang Y, Gao H, Hwang KC. Strain-gradient plasticity at the micron scale. In: Ellyin F, Provan JW, editors. *Progress in mechanical behavior of materials proceedings of ICM-8, vol. III*. Victoria, BC: Fleming; 1999. p. 1051–6.
70. Becker R. Nucleus formation in the separation of metallic mixed crystals. *Ann Phys* 1938;**32**:128–40.
71. Lee YW, Aaronson HI. Anisotropy of coherent interphase boundary energy. *Acta Metall* 1998;**28**:539–48.
72. Borchers C, Bormann R. Determination of low-temperature interfacial energies from a pair interaction model. *Acta Mater* 2005;**53**:3695–701.
73. Finnis MW. The theory of metal–ceramic interfaces. *J Phys Condens Matter* 1996;**8**:5811–36.
74. Batyrev IG, Alavi A, Finnis MW. Equilibrium and adhesion of Nb/sapphire: the effect of oxygen partial pressure. *Phys Rev B* 2000;**62**:4680–706.
75. Bennet IJ, Kranenburg JM, Sloof WG. Modeling the influence of reactive elements on the work of adhesion between oxides and metal alloys. *J Am Ceram Soc* 2005;**88**:2209–16.
76. Siegel DJ, Hector Jr LG, Adams JB. Adhesion, stability and bonding at metal/metal-carbide interfaces: Al/WC. *Surf Sci* 2002;**498**:321–36.
77. Siegel DJ, Hector Jr LG, Adams JB. First-principles study of metal-carbide/nitride adhesion: Al/VC vs. Al/VN. *Acta Mater* 2002;**50**:619–31.
78. Raynolds JE, Roddick RE, Smith JR, Srolovitz DJ. Impurity effects on adhesion at an interface between NiAl and Mo. *Acta Mater* 1999;**47**:3281–9.
79. Lipkin DM, Israelachvili JN, Clarke DR. Estimating the metal–ceramic van der Waals adhesion energy. *Philos Mag A* 1997;**73**:715–28.
80. Van Swygenhoven, Spaczer HM, Caro A. Microscopic description of plasticity in computer generated metallic nanophase samples: a comparison between Cu and Ni. *Acta Mater* 1999;**47**:3117–26.
81. Hoagland RG, Kurtz RJ, HenagerF C.H. Jr. Slip resistance of interfaces and the strength of metallic multilayer composites. *Scr Mater* 2004;**50**:775–9.
82. Gerberich WW, Oriani RA, Lii MJ, Chen X, Foeke T. The necessity of both plasticity and brittleness in the fracture thresholds of iron. *Philos Mag A* 1991;**63**:363–76.
83. Hirsch PB, Roberts SG, Samuels J. The dynamics of dislocation generation at crack-tips and the ductile–brittle transition. *Scr Metall* 1987;**21**:11523–8.
84. Voronoi GJ. New parametric applications concerning the theory of quadratic forms—second announcement. *J Reine Angew Math* 1908;**134**(1/4):198–287.
85. Tadmor EB, Ortiz M, Phillips R. Quasicontinuum analysis of defects in solids. *Philos Mag A* 1996;**73**:1529–63.
86. Miller R, Tadmor EB, Phillips R, Ortiz M. Quasicontinuum simulation of fracture at the atomic scale. *Modell Simul Mater Sci Eng* 1998;**6**:607–38.
87. Curtin WA, Miller RE. Atomistic/continuum coupling in computational materials science. *Modell Simul Mater Sci Eng* 2003;**11**:R33–68.
88. Thomson R. Physics of fracture. *Solid State Phys* 1986;**39**:1–129.
89. Thomson RM. Physics of fracture. *J Phys Chem Solids* 1987;**48**:965–83.
90. Atkinson C, Clements DL. The influence of anisotropy and crystalline slip on relaxation at a crack tip. *Acta Metall* 1973;**21**:55–60.
91. Lii MJ, Gerberich WW. The stress state close to a crack tip shielded by a dislocation array. *Scr Metall* 1988;**22**:1779–82.
92. Gerold AW, Ronald DN. Analysis of asperity–asperity adhesion forces utilizing statistical analysis techniques and the force selectivity of the scanning probe microscope. *Langmuir* 2002;**18**(22):8370–4.
93. Ibrahim TH, Burk TR, Etzler FM, Neuman RD. Direct adhesion measurements of pharmaceutical particles to gelatine capsule surface. *J Adhes Sci Technol* 2000;**14**:1225–42.
94. Giesbers M, Kleijn JM, Fleer GJ, Cohen Stuart MA. Forces between polymer-covered surfaces: a colloidal probe study. *Colloids Surf A* 1998;**142**:343–53.
95. Rutland MW, Carambassis A, Willing GA, Neuman RD. Surface force measurements between cellulose surfaces using scanning probe microscopy. *Colloids Surf A: Physicochem Eng Aspects* 1997;**123**:369–74.
96. Ott ML, Mizes HA. Atomic force microscopy adhesion measurements of surface-modified toners for xerographic applications. *Colloids Surf A: Physicochem Eng Aspects* 1994;**87**(3):245–56.
97. Gerberich WW, Cordill MJ. Physics of adhesion. *Rep Progr Phys* 2006;**69**:2157–203.
98. Wang HR, Gerberich WW, Skowronek CJ. Fracture mechanics of Ti/Al_2O_3 interfaces. *Acta Metall Mater* 1993;**41**:2425–32.
99. Venkataraman SK, Kohlstedt DL, Gerberich WW. Metal–ceramic interfacial fracture resistance using the continuous microscratch technique. *Thin Solid Films* 1993;**223**:269–75.
100. Cooper K, Gupta A, Beaudoin SJ. *Colloid Interface Sci* 2001;**234**:284–92.
101. Larson I, Drummond CJ, Chan DYC, Grieser F. *Langmuir* 1997;**13**:2109–12.
102. Muir I, Meagher L, Gee M. Interaction forces between α-alumina fibers with coabsorbed polyelectrolyte and surfactant. *Langmuir* 2001;**17**:4932–9.
103. Gotzinger M, Peukert W. Dispersive forces of particle-surface interactions: direct AFM measurements and modelling. *Powder Technol* 2003;**130**:102–9.
104. Heim LO, Blum J, Preuss M, Butt HJ. Adhesion and friction forces between spherical micrometer-sized particles. *Phys Rev Lett* 1999;**83**:3328–31.
105. Bausch AR, Bowick MJ, Cacciuto A, Dinsmore AD, Hsu MF, Nelson DR, et al. Grain boundary scars and spherical crystallography. *Science* 2003;**299**:1716–8.
106. Israelachvili JN. *Intermolecular and Surface Forces*. 2nd ed. London: Academic Press; 1992. p. 326–8.

107. Götzinger M, Peukert W. Adhesion forces of spherical alumina particles on ceramic substrates. *J Adhes* 2004;**80**:223–42.
108. Rumpf H, Sommer K, Steier K. Mechanismen der Haftkraftverstärkung bei der Partikelhaftung durch plastisches Verformen, Sintern und viskoeslastisches Flieβen. *Chem Ing Tech* 1976;**48**(4):300–7.
109. Landman U, Luedke WD, Gao J. Measuring tip shape for instrumented indentation using the atomic force microscopy. *Langmuir* 1996;**12**:4514–28.
110. ISO group TC 164/SC 3/WG 1, ASTM E28.06.11. Metallic materials-Instrumented indentation test for hardness and materials parameters, ISO/DIS 14577-1, 2, and 3.
111. Jabbour ZL, Yaniv SL. The kilogram and the measurements of mass and force. *J Res Natl Inst Stand Technol* 2001;**106**:25–46.
112. Williams ER, Steiner RL, Newell DB, Olsen PT. Accurate measurement of the Planck constants. *Phys Rev Lett* 1998;**81**:2404–7.
113. Funck T, Sienknecht V. Determination of the Volt with the improved PTB voltage balance. *IEEE Trans Inst Meas* 1991;**40**:158–61.
114. Jennett NM, Meneve J. Depth sensing indentation of thin hard films: a study of modulus measurement sensitivity to indentation parameters. In: Moody NR, Gerberich WW, Burnham N, Baker SP, editors. *Fundamentals of nanoindentation and nanotribology*, vol. 522. Pittsburgh, PA: Materials Research Society; 1998. p. 239–44.
115. Meneve JL, Smith JF, Jennett NM, Saunders RSJ. Surface mechanical property testing by depth sensing indentation. *Appl Surf Sci* 1998;**100/101**:64–8.
116. VanLandingham MR, Villarrubia JS, Meyers GF. Recent progress in nanoscale indentation of polymers using the AFM. In: *Proceedings of the SEM IX international congresson experimental mechanics*. Betherl, CT: Society for Engineering Mechanics, Inc.; 2000. p. 912–5.
117. VanLandingham MR, Villarrubia JS, Camara R. Measuring tip shape for instrumented indentation using the atomic force microscope. *J Mater Res* 2003.
118. McElhaney KW, Vlassak JJ, Nix WD. Determination of indenter tip geometry and indentation contact area for depth-sensing indentation experiments. *J Mater Res* 2002;**13**:1300–6.
119. Thurn J, Cook RF. Simplified area function for sharp indenter tips in depth-sensing indentation. *J Mater Res* 2002;**17**:1143–6.
120. Sun Y, Zheng S, Bell T, Smith J. Indenter tip radius and load frame compliance calibration using nanoindentation loading curves. *Philos Mag Lett* 1999;**79**:649–58.
121. Oliver WC, Phar GM. Measurement of hardness and elastic modulus by instrumented indentation: advances in understanding and refinements to methodology. *J Mater Res* 2004;**19**:3–20.
122. Field JS, Swain MV. A simple predictive model for spherical indentation. *J Mater Res* 1993;**8**:297–306.
123. Field JS, Swain MV. Determining the mechanical properties of small volumes of material from submicrometer spherical indentations. *J Mater Res* 1995;**10**:101–12.
124. Namazu T, Isono Y. Quasi-static bending test of nano-scale SiO_2 wire at intermediate temperatures using AFM-based technique. *Sens Actuators A* 2003;**104**:78–85.
125. Oliver WC, Pharr GM. An improve technique for determining hardness and elastic modulus using load and displacement sensing indentation experiments. *J Mater Res* 1992;**7**:1564–83.
126. Çagin T, Che J, Gardos MN, Fijany A, Goddard III WA. Simulation and experiments on friction and wear of diamond: a material for MEMS and NEMS application. *Nanotechnology* 1999;**10**:278–84.
127. Erdemir A, Donnet C. In: Bhushan B, editor. *Modern Tribology Handbook*, vol. 2. Boca Raton: CRC Press; 2001. p. 465.
128. Krauss AR, Auciello O, Gruen DM, Jayatissa A, Sumant A, Tucek J, et al. Ultrananocrystalline diamond thin films for MEMS and moving mechanical assembly devices. *Diam Relat Mater* 2001;**10**:1952–61.
129. Sekaric L, Parpia JM, Craighead HG, Feygelson T, Houston BH, Butler JE. Nanomechanical resonant structures in nanocrystalline diamond. *Appl Phys Lett* 2002;**81**:4455–7.
130. Gardos MN. Surface chemistry-controlled tribological behaviour of Si and diamond. *Tribol Lett* 1996;**2**:173–87.
131. Van den Oetelaar RJA, Flipse CFJ. Atomic-scale friction on diamond (1 1 1) studied by ultra-high vacuum atomic force microscopy. *Surf Sci* 1997;**384**:1828–35.
132. Gao GT, Mikulski PT, Harrison JA. Molecular-scale tribology of amorphous carbon coatings: effects of film thickness, adhesion, and long-range interactions. *J Am Chem Soc* 2002;**124**:7202–9.
133. Qi Y, Konca E, Alpas AT. Atmospheric effects on the adhesion and friction between non-hydrogenated diamond-like carbon (DLC) coating and aluminium—a first principles investigation. *Surf Sci* 2006:2955–65.
134. Gardos MN. Protective coatings and thin films, In: Pauleau Y, Barna PB, editors. *Proc. NATO adv. res. workshop. NATO ARW Series*. Dordrecht: Kluwer; 1996, p. 185.
135. Germann GJ, Cohen SR, Neubauer G, McClelland GM, Seki H. Atomic scale friction of a diamond tip on diamond (1 0 0) and (1 1 1) surfaces. *J Appl Phys* 1992;**73**:163–7.
136. Perry MD, Harrison JA. Friction between diamond surfaces in the presence of small third-body molecules. *J Phys Chem B* 1997;**101**: 1364–73.
137. Gao G, Cannara RJ, Carpick RW, Harrison JA. Atomic-scale friction on diamond: a comparison of different sliding directions on (0 0 1) and (1 1 1) surfaces using MD and AFM. *Langmuir* 2007;**23**:5394–405.
138. Sumant AV, Grierson DS, Gerbi JE, Birrell J, Lanke UD, Auciello O, et al. Toward the ultimate tribological interface: surface chemistry and nanotribology of ultrananocrystalline diamond. *Adv Mater* 2005;**17**:1039–45.
139. Erdemir A, Bindal C, Fenske GR, Zuiker C, Csencsits R, Krauss AR, et al. *Diam Films Technol* 1996;**6**:31.
140. Heimberg JA, Wahl KJ, Singer IL, Erdemir A. Superlow friction behaviour of diamond-like carbon coatings: time and speed effects. *Appl Phys Lett* 2001;**78**:2449–51.
141. Enachescu M, Van den Oetelaar RJA, Carpick RW, Ogletree DF, Flipse CFJ, Salmeron M. Atomic force microscopy study of an ideally hard contact: the diamond (1 1 1)/tungsten carbide interface. *Phys Rev Lett* 1998;**81**:1877–80.
142. Corbella C, Vives M, Oncins G, Canal C, Andújar JL, Bertran E. Characterization of DLC films obtained at room temperature by pulsed-dc PECVD. *Diam Relat Mater* 2004;**13**:1494–9.
143. Riedo E, Chevrier J, Comin F, Brune H. Nanotribology of carbon base thin films: the influence of film structure and surface morphology. *Surf Sci* 2000;**477**:25–34.
144. Fang T-H, Weng C-I, Chang J-G, Hwang C-C. Nanotribology of amorphous hydrogenated carbon films using scanning probe microscopy. *Thin Solid Films* 2001;**396**:166–72.
145. Gao GT, Mikulski PT, Chateauneuf GM, Harrison JA. The effect of film structure and surface hydrogen on the properties of amorphous carbon films. *J Phys Chem B* 2003;**107**:11082–90.
146. Gang H, Müser MH, Robbins MO. Adsorbed layers and the origin of static friction. *Science* 1999;**284**:1650–2.
147. Kim HI, Lince JR, Eryilmaz OL, Erdemir A. Environmental effects on the friction of hydrogenated DLC films. *Tribol Lett* 2006;**21**:53–8.
148. Konicek AR, Grierson DS, Gilbert PUPA, Sawyer WG, Sumant AV, Carpick RW. Origin of ultralow friction and wear in ultrananocrystalline diamond. *Phys Rev Lett* 2008;**100**:235502.
149. Sun L, Wu Q. Transformation probability of graphite-diamond assisted by non-metallic catalysts at high pressure and high temperature. *J Mater Res* 1998;**14**:631–3.
150. Qi Y, Konca E, Aplas AT. Atmospheric effects on the adhesion and friction between non-hydrogenated diamond-like carbon (DLC) coating and aluminum—a first principles investigation. *Surf Sci* 2006;**600**:2955–65.
151. Andersson P, Juhanko J, Nikkilä A-P, Lintula P. Influence of topography on the running-in of water-lubricated silicon carbide journal bearings. *Wear* 1996;**201**:1–9.
152. Hornetz B, Michel HJ, Halbritter J. ARXPS studies of SiO_2–SiC interfaces and oxidation of 6H SiC single-crystal Si-(0 0 1) and C-(0 0 1) interfaces. *J Mater Res* 1994;**9**:3088–94.
153. Lavrenko VA, Jonas S, Pampuch R, Petrographic and X-ray identification of phases formed by oxidation of silicon carbide. *Ceram Int* 1981;**7**:75–6.
154. Rahaman MN, De Jonghe LC. Angle-resolved XPS analysis of oxidized polycrystalline SiC surfaces. *Am Ceram Soc Bull* 1987;**66**:782–5.

155. Pöhlmann K, Bhushan B, Gahr K-HZ. Effect of thermal oxidation on indentation and scratching of single-crystal silicon carbide on microscale. *Wear* 2000;**237**:116–28.
156. Noreyan A, Amar JG, Marinescu I. Molecular dynamics simulations of nanoindentation of β-SiC with diamond indenter. *Mater Sci Eng B* 2005;**117**:235–40.
157. Noreyan A, Amar JG. Molecular dynamics simulations of nanoscratching of 3C SiC. *Wear* 2008;**265**:956–62.
158. Heshmat H, Jahanmir S. Tribological behaviour of ceramics at high sliding speeds in steam. *Tribol Lett* 2004;**17**:359–66.
159. O'Regan B, Grätzel M. A low-cost, high-efficiency solar cell based on dye-sensitized colloidal TiO_2 films. *Nature* 1991;**353**:737–40.
160. Sousa SR, Moradas-Ferreira P, Saramago B, Viseu Melo L, Barbosa MA. Human serum albumin adsorption on TiO_2 form single protein solutions and from plasma. *Langmuir* 2004;**20**:9745–54.
161. Jämting AK, Bell JM, Swain MV, Wielunski LS, Clissold R. Measurement of the micro mechanical properties of sol–gel TiO_2 films. *Thin Solid Films* 1998;**332**:189–94.
162. Zang W, Liu W, Wang C. Tribological behaviour of sol–gel TiO_2 films on glass. *Wear* 2002;**253**:377–84.
163. Piwonski I. Preparation method and some tribological properties of porous titanium dioxide layers. *Thin Solid Films* 2006;**515**:3499–506.
164. Scandella L, Meyer E, Howald L, Lüthi R, Guggisberg M, Gobrecht J, et al. Friction forces on hydrogen passivated (1 1 0) silicon and silicon dioxide studied by scanning force microscopy. *J Vac Sci Technol B* 1996;**14**:1255–8.
165. Kern W. *Handbook of semiconductor cleaning and technology*. Park Ridge, NJ: Noyes; 1993.
166. Belyi VI, Vasilyeva LL, Ginovker AS, Gritsenko VA, Repinsky SM, Sinitsa SP, et al. *Silicon nitride in electronics materials science monographs no. 34*. Amsterdam: Elsevier; 1988.
167. Fischer TE, Tomizawa H. Interaction of tribochemistry and microfracture in the friction and wear of silicon nitride. *Wear* 1995;**105**:29–45.
168. Gabriel KJ, Behi F, Mahadevan R, Mehregany M. In situ friction and wear measurements in integrated polysilicon mechanisms. *Sens Actuators A* 1990;**21–23**:184–8.
169. Tai Y, Muller RS. Frictional study of IC-processed micromotors. *Sens Actuators A* 1990;**21–23**:180–3.
170. Binggeli M, Mate CM. Influence of water vapour on nanotribology studied by friction force microscopy. *J Vac Sci Technol B* 1995;**13**:1312–5.
171. Opitz A, Ahmed SIU, Schaefer JA, Scherge M. Friction of thin water films: a nanotribological study. *Surf Sci* 2002;**504**:199–207.
172. Halbritter J. Charge transfer via interfaces especially of nanoscale materials. *Appl Phys A* 1999;**68**:153–62.
173. Sokolov IY, Henderson GS, Wicks FJ, Ozin GA. Improved atomic force microscopy resolution using an electric double layer. *Appl Phys Lett* 1997;**70**:844–6.
174. Persson BNJ. *Sliding friction: physical principles and applications*. Berlin: Springer-Verlag; 2000.
175. Opitz A, Ahmed SIU, Schaefer JA, Scherge M. Nanofriction of silicon oxide surfaces covered with thin water films. *Wear* 2003;**254**:924–9.
176. Bhushan B, Gupta BK, Azarian MH. *Wear* 1995;**181–183**:743.
177. Gee MG, Jennett NM. *Wear* 1995;**193**:133.
178. Xie H, Song K, Mann DJ, Hase WL. *Phys Chem Chem Phys* 2002;**4**:5377.
179. Ziebert C, Zum Gahr KH. Microtribological properties of two-phase Al_2O_3 ceramic studied by AFM and FFM in air of different relative humidity. *Tribol Lett* 2004;**17**(4):901–8.
180. Israelachvili JN, Intermolecular. *Surface forces*. 2nd ed. London: Academic Press; 1991.
181. Raviv U, Klein J. Fluidity of bound hydration layers. *Science* 2002;**297**:1540–3.
182. Yilmaz H, Sato K, Watari K. AFM interaction study of α-alumina particle and c-sapphire surfaces at high-ionic-strength electrolyte solutions. *J Colloid Interface Sci* 2006;**307**:116–23.
183. Donose BC, Vakarelski IU, Higashitani K. Silica surfaces lubrication by hydrated cations adsorption from electrolyte solutions. *Langmuir* 2005;**21**:1834–9.
184. Vakarelski IU, Higashitani K. Dynamic features of short-range interaction force and adhesion in solutions. *J Colloid Interface Sci* 2001;**242**:110–20.
185. Sedin DL, Rowlen KL. Adhesion forces measured by atomic force microscopy in humid air. *Anal Chem* 2000;**72**(10):2183–9.
186. Butt H-J. Measuring electrostatic, van der Waals, and hydration forces in electrolyte solutions with an atomic force microscope. *J Biophys* 1991;**60**:1438–44.
187. Leite FL, Ziemath EC, Oliveira Jr ON, Herrmann PSP. Adhesion force for mica and silicon oxide surfaces studied by atomic force microcopy (AFS). *Microsc Microanal* 2005;**11**(supp 3).
188. Johnson KL. Contact mechanics and adhesion of viscoelastic solids. In: *Book of abstracts. 216th ACS national meeting*. 1998.
189. Fuller KNG, Tabor D. The effect of surface roughness on the adhesion of elastic solids. *Proc R Soc Lond A* 1975;**345**:327–42.
190. Pöhlmann K, Zlum Gahr K-H. AFM-Untersuchugen zu adhäsiven Wechselwirkungen an einkristallinem Si und voroxidiertem SiC in Abhängigkeit von der relativen Lufffeuchte. *Mater Sci Eng Technol* 2000;**31**(4):280–9.
191. Zum Garh K-H, Blattner R, Hwanf D-H, Pöhlmann K. Micro- and macro-tribological properties of SiC ceramics in sliding contact. *Wear* 2001;**250**:299–310.
192. Binggeli M, Mate CM. Influence of water vapour on nanotribology studied by friction force microscopy. *J Vac Sci Technol B: Microelectron Nanometer Struct* 1995;**13**(3):1312–5.
193. Zou M, Cai L, Wanga H. Adhesion and friction studies of a nano-textured surface produced by spin coating of colloidal silica nanoparticle solution. *Tribol Lett* 2006;**21**(1):25–30.
194. Yoon E, Yang SH, Han H, Kong H. An experimental study on the adhesion at a nano-contact. *Wear* 2003;**254**:974–80.
195. Hamaker HC. The London-can der Waals attraction between spherical particles. *Physica* 1937;**4**(10):1058–72.
196. Yang Y, Sigmund WM. Rheological properties and gelation threshold of temperature induced forming (TIF) alumina suspensions with variation in molecular weight of polyacrylic acid. *J Mater Synth Process* 2002;**10**(5):249–55.
197. Ducker WA, Senden TJ, Pashley RM. Measurement of forces in liquids using a force microscope. *Lagmuir* 1992;**8**:1831–6.
198. Kirkham J, Brookes SJ, Shore RC, Bonass WA, Smith DA, Wallwork ML, et al. Atomic force microscopy studies of crystal surface topology during enamel development. *Connect Tissue Res* 1998;**38**(1–4):91–100.
199. Kirkham J, Zhang J, Brookes SJ, Shore RC, Ryu OH, Wood SR, et al. Evidence for change domains on developing enamel crystal surfaces. *J Dent Res* 2000;**79**(12):1943–7.
200. Robinson C, Connell S, Brookes SJ, Kirkham J, Shore RC, Smith AM. The effect of fluoride on the developing tooth. *Caries Res* 2004;**38**(3):268–76.
201. Folch A, Gorostiza P, Serva J, Tejada J, Sanz F. Enhanced surface atomic step motion observed in real time after nanoindentation of NaCl (1 0 0). *Surf Sci* 1997;**380**(2/3):427–33.
202. Aselage T, Keefer K. Liquidus relations in Y–Ba–Cu oxides. *J Mater Res* 1988;**3**:1279–91.
203. Sandiumenge F, Puig T, Rabier J, Plain J, Obradors X. Optimization of flux pinning in bula melt textured 1-2-3 superconductors. Bringing dislocations under control. *Adv Mater* 2000;**12**(5):375–81.
204. Licci F, Gauzzi A, Marezio M, Radaelli GP, Masini R, Chaillout-Bougerol C. Structural and electronic effects of Sr substitution for Ba in $Y(Ba_{1-x}Sr_x)_2Cu_3O_w$ at varying *w*. *Phys Rev B: Condens Matter Mater Phys* 1998;**58**(22):15208–17.
205. Roa JJ, Capdevila XG, Martínez M, Espiell F, Segarra M. Nanohardness and Young's modulus of YBCO samples textured by the Bridgman technique. *Nanotechnology* 2007;**18**:385701/1–6.

Glossary

A: Contact area.
a: Contact of one solid.
αδ: Interphase.

β: Contact of an environment.
$\beta\delta$: Interphase.
dW: Change in energy.
dz: Change in the overlap or separation of the electrodes.
dC: Change in capacitance.
dC/dz: Capacitance gradient.
δ: Penetration depth.
Δ: Cantilever deflection.
ΔV: Increment in photodetector vertical signal.
E: Young's modulus.
F_a: Adhesion force.
F_v: Applied vertical force.
F_f: Friction force.
$\gamma^{f,s}$: Surface energies of the film and substrate.
H: Hardness.
γ: Surface energies for materials.
δ: Penetration depth.
m_s: Mass of the slider.
μ: Friction coefficient.
F_a: Adhesion force.
R: AFM tip radius.
S: Stiffness.
σ_{ys}: Yield strength.
ν: Poisson ratio.
V: Electric potential across the capacitor.
W_a: Work of adhesion.
SFA: Surface force apparatus.
SNPT: Silica nanoparticle textured.
SOF: Silicon oxide films.
AFM: Atomic force microscopy.
ASTM: American Section of the International Association for Testing Materials.
ISO: International Organization for Standardization.
QCM: Quartz crystal microbalance.
MEMS: Microelectromechanical system.
NEMS: Nanoelectromechanical system.
SEM: Scanning electron microscopy.
SI: International Systems.
DFT: Density functional theory.
MD: Molecular dynamics.
UNCD: Ultrananocrystalline diamond.
DLC films: Diamond-like carbon films.
MPCVD: Microwave plasma chemical vapour deposition.
PLD: Pulsed laser deposition.
NEXAFS: X-ray absorption fine structure.
X-PEEM: X-ray photoelectron emission microscopy.
EDL: Electrostatic double layer.
CFM: Chemical force microscopy.